Beamforming for Sensing: Hybrid Beamforming based on Transmitter-Receiver Collaboration for Millimeter-Wave Sensing

LONG FAN, State Key Laboratory for Novel Software Technology, Nanjing University, China
LEI XIE*, State Key Laboratory for Novel Software Technology, Nanjing University, China
WENHUI ZHOU, State Key Laboratory for Novel Software Technology, Nanjing University, China
CHUYU WANG, State Key Laboratory for Novel Software Technology, Nanjing University, China
YANLING BU, College of Computer Science and Technology, Nanjing University of Aeronautics and Astronautics, China
SANGLU LU, State Key Laboratory for Novel Software Technology, Nanjing University, China

Previous mmWave sensing solutions assumed good signal quality. Ensuring an unblocked or strengthened LoS path is challenging. Therefore, finding an NLoS path is crucial to enhancing perceived signal quality. This paper proposes *Trebsen*, a Transmitter-REceiver collaboration-based Beamforming scheme SENsing using commercial mmWave radars. Specifically, we define the hybrid beamforming problem as an optimization challenge involving beamforming angle search based on transmitter-receiver collaboration. We derive a comprehensive expression for parameter optimization by modeling the signal attenuation variations resulting from the propagation path. To comprehensively assess the perception signal quality, we design a novel metric *perceived signal-to-interference-plus-noise ratio (PSINR)*, combining the carrier signal and baseband signal to quantify the fine-grained sensing motion signal quality. Considering the high time cost of traversing or randomly searching methods, we employ a search method based on deep reinforcement learning to quickly explore optimal beamforming angles at both transmitter and receiver. We implement *Trebsen* and evaluate its performance in a fine-grained sensing application (i.e., heartbeat). Experimental results show that *Trebsen* significantly enhances heartbeat sensing performance in blocked or misaligned LoS scenes. Comparing non-beamforming, *Trebsen* demonstrates a reduction of 23.6% in HR error and 27.47% in IBI error. Moreover, comparing random search, *Trebsen* exhibits a 90% increase in search speed.

CCS Concepts: • **Computer systems organization → Embedded and cyber-physical systems**; • **Human-centered computing → Ubiquitous and mobile computing systems and tools**.

Additional Key Words and Phrases: mmWave Radar, Fine-grained Motion Sensing, Hybrid Beamforming

ACM Reference Format:
Long Fan, Lei Xie, Wenhui Zhou, Chuyu Wang, Yanling Bu, and Sanglu Lu. 2024. Beamforming for Sensing: Hybrid Beamforming based on Transmitter-Receiver Collaboration for Millimeter-Wave Sensing. *Proc. ACM Interact. Mob. Wearable Ubiquitous Technol.* 8, 2, Article 75 (June 2024), 27 pages. https://doi.org/10.1145/3659619

*Lei Xie is the corresponding author.

Authors' addresses: Long Fan, State Key Laboratory for Novel Software Technology, Nanjing University, Nanjing, China, fanl@smail.nju.edu.cn; Lei Xie, State Key Laboratory for Novel Software Technology, Nanjing University, Nanjing, China, lxie@nju.edu.cn; Wenhui Zhou, State Key Laboratory for Novel Software Technology, Nanjing University, Nanjing, China, zhouwh2000@foxmail.com; Chuyu Wang, State Key Laboratory for Novel Software Technology, Nanjing University, Nanjing, China, chuyu@nju.edu.cn; Yanling Bu, College of Computer Science and Technology, Nanjing University of Aeronautics and Astronautics, Nanjing, China, byling@nuaa.edu.cn; Sanglu Lu, State Key Laboratory for Novel Software Technology, Nanjing University, Nanjing, China, sanglu@nju.edu.cn.

ACM 2474-9567/2024/6-ART75
https://doi.org/10.1145/3659619

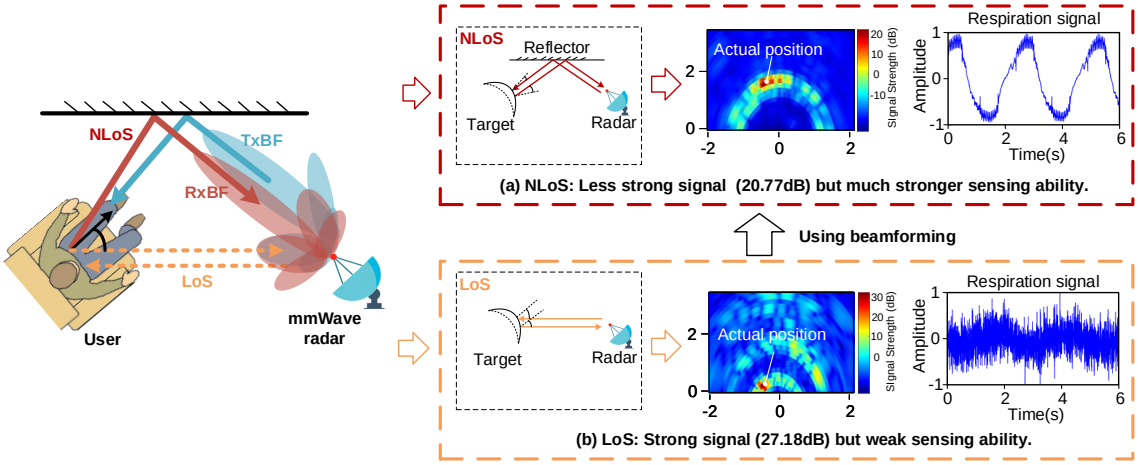

Fig. 1. Illustration of the application of *Trebsen* for enhancing mmWave sensing capabilities.

1 INTRODUCTION

With the rapid advancement of millimeter-wave (mmWave) technology, researchers have developed a large number of revolutionary mmWave-based sensing applications to serve daily life, e.g., health monitoring [27], voice sensing [12, 13], gesture recognition [20, 21], and handwriting tracking [31]. These mmWave-based sensing solutions can usually perform well in the ideal environment, because the line-of-sight (LoS) communication between the sensing target and the mmWave radar can be guaranteed. However, in practical circumstances, the quality of fine-grained perception signals through the LoS path may degrade because the transmission direction of the mmWave radar signal and the motion direction of the sensing target may be misaligned, as illustrated in Fig.1(b). In this case, it is difficult for traditional methods to effectively extract high-quality fine-grained motion signals, even if the carrier energy of LoS is strong. Such a situation becomes universal when sensing fine-grained motion like speech or heartbeat. Previous works have typically assumed that the optimal sensing path is LoS. However, our findings indicate that the essential factor influencing the quality of fine-grained motion signals is the relationship between the transmission direction of the mmWave radar and the motion direction of the sensing target. As illustrated in Fig.1(a), aligning the transmission direction of the mmWave radar with the motion direction of the sensing target, even in a Non-Line of Sight (NLoS) scenario, results in improved signal quality for fine-grained motion. Therefore, finding an optimal sensing path is crucial for enhancing the quality of fine-grained motion signals.

Aiming at improving the robustness and accuracy of fine-grained mmWave-based sensing, existing work can be divided into machine learning-based feature extraction and beamforming-based feature fusion to improve the signal quality. On the one hand, machine learning-based solutions focus on exploring advanced signal processing approaches to extract efficient features [12, 26] or multi-modal sensing [23, 24]. However, they are often tailored to specific applications and require that the original quality of the received signal is not too poor. On the other hand, as the diffraction ability of mmWave is weak, beamforming technology is an effective way to improve the mmWave signal quality fundamentally [28] and serve a wide range of applications. However, existing methods [5, 37] were primarily designed to enhance the communication signal quality, often overlooking perception signal quality in fine-grained sensing scenarios. Here, the communication signal quality refers to signal strength, where the absolute receiving signal power can be guaranteed by the beamforming. In the contract, the perception signal quality refers to quantifying fine-grained motion variation, which is seldom discussed in the existing solutions. Besides, since the location of the sensing target is usually unknown in the sensing field,

previous study [36] merely use the receiver beamforming (RxBF) to improve positioning estimation accuracy. They neglect the importance of utilizing transmitter beamforming (TxBF) to improve transmitter power.

In this paper, we propose *Trebsen*, a Transmitter-REceiver collaboration-based Beamforming scheme SENsing using commercial mmWave radars, to efficiently improve the perception signal quality. In particular, considering that there leads to a lower perception signal quality in the LoS blocked or misaligned scenarios, our basic idea is to search for an optimal NLoS path with a strong perception signal quality, and then steer both the transmitting and receiving antenna array to the direction of the optimal path with beamforming for feature extraction, as shown in Fig. 1. Specifically, we build an optimal propagation path sensing model to describe the relationship between the propagation path and the signal quality, which guarantees the existence of such an optimal path. Traditionally, we can try each angle combination iteratively and then judge the performance of such an angle combination for optimal path searching. Therefore, there needs to be a metric to quantify the performance of fine-grained sensing efficiently. To assess the signal quality comprehensively, we design a novel metric *perceived signal-to-interference-plus-noise ratio (PSINR)*, including *carrier-energy-to-noise ratio (CENR)* and *baseband entropy*. Here, *CENR* measures the signal power of the target position, which indicates the communication signal quality, while *baseband entropy* measures the frequency-band power of target movement, which indicates the perception signal quality. Our proposed PSINR serves as a perceptual signal quality evaluation index for assessing the received signal quality. Moreover, considering the high time cost of traversing or randomly searching all angle combinations. We propose to leverage deep reinforcement learning (DRL) to automatically search for the optimal path quickly via an adaptive parameter search method, which uses *PSINR* as a reward and received signals as observations input. Based on the optimal path, we simply steer both the transmitting and receiving antenna arrays to the direction via hybrid beamforming to obtain better signal features for target sensing.

There are three major challenges in improving the signal quality for fine-grained motion sensing. *1) How to quantify perceptual signal quality?* Perception based on mmWave radar is widely used, especially fine-grained perception such as speech or heartbeat signals. However, existing metrics, e.g., signal-to-noise ratio (SNR), can only assess the energy intensity, neglecting the signal variance for fine-grained motion sensing. Moreover, we observed that in some scenarios, especially when the LoS path is misaligned, the previous energy-based SNR could not describe the fine-grained motion signal quality. Therefore, how to effectively quantify the quality of fine-grained perception signals is particularly important. To address this challenge, we design a novel metric *PSINR* to comprehensively depict both the energy intensity and signal variance. In particular, *PSINR* constructs a two-dimensional quantization matrix based on *CENR* and *baseband entropy*. Here, *CENR* measures the energy intensity distribution of the space, while *baseband entropy* measures the signal variance feature, which focuses on the target frequency band with respect to the fine-grained motion. Thus, we can use *CENR* to determine whether there is a target reflection and then leverage *baseband entropy* to further determine whether there is a fine-grained motion as expected. For example, for the respiration monitoring, *baseband entropy* measures the signal variance power of $0.3 - 0.8$ Hz frequency band. It can be used to determine whether there is a target respiration signal or only a static reflection signal.

2) How to balance signal propagation losses to maximize perceived signal quality? In practice, the fine-grained sensing performance decreases severely when the LoS path is blocked, or the directions between the target movement and the propagation are misaligned (i.e., signal weakened). We observe that the path length, the angle between the incident signal and the target motion vector, etc., all impact the perceived signal. Therefore, how to balance the loss of path length, incidence/reflection angle, etc., to provide a high-quality signal for fine-grained perception? To address this challenge, we build an optimal propagation path sensing model to demonstrate the relationship between signal quality and the signal propagation losses when sensing fine-grained motion. The model decomposes the received signal into multiple components according to the propagation paths, and it explains the target movement impact on the signal quality of each propagation path with respect to the incidence/reflection angle. This model ascertains the feasibility of constructing an optimal signal propagation path to improve the

signal quality, which can be either the LoS path or an NLoS path according to the incidence/reflection angle. Therefore, in a harsh environment, when it is impossible to obtain high-quality signals via LoS path for fine-grained sensing, we can effectively find an optimal NLoS path with high quality. Then, we can leverage a hybrid-beamforming method of transmitter-receiver collaboration to enhance both the transmitting signal, and receiving signal of the optimal path while weakening the signal of other paths to improve the signal quality.

3) How to obtain the hybrid beamforming angles quickly? Traditionally, we can try each TxBF and RxBF angle combination iteratively and then use *PSINR* to judge the performance of such an angle combination for optimal path searching. However, considering the high time cost of traversing or randomly searching all angle combinations, the performance of its search results cannot be guaranteed. Therefore, designing a fast and effective optimal hybrid beamforming angles search method is crucial. To address this challenge, we propose a DRL-based search method to quickly search for optimal hybrid beamforming angles while guaranteeing perceptual signal quality, instead of brute force traversal. Specifically, to quickly estimate the hybrid beamforming angles, we design a generation network, that uses the received signal of the antenna array as input to estimate the angle combination. To evaluate the value of the generated beamforming angles, we designed a value evaluation network to evaluate the value of the beamforming angle and the received signal. To ensure the generation network converges quickly and obtains the optimal beamforming angle within the minimum number of search steps, we use the quantification metric *PSINR* to train the evaluation network, which is further used via a reinforcement learning framework to train the generation network.

We make three key contributions in this paper. Firstly, we propose *Trebsen*, a Transmitter-REceiver collaboration-based Beamforming scheme SENsing using commercial mmWave radars, to efficiently improve the perception signal quality. It has the capability to autonomously create an optimal signal propagation path by dynamically adjusting both transmitting beamforming and receiving beamforming. Even if the LoS path is blocked or misaligned, it can ensure a high signal quality to effectively sense fine-grained target motion. Secondly, we design a novel metric *PSINR*, which constructs a two-dimensional quantization matrix based on *CENR* and *baseband entropy* to assess the signal quality comprehensively. By using *PSINR* as a reward, we employ a DRL-based parameter search method to quickly determine the optimal hybrid beamforming angles at both transmitter and receiver. Thirdly, we have implemented *Trebsen* and evaluated its performance at the scheme level and in a specific fine-grained sensing application, i.e., heartbeat monitoring. Experimental results show that *Trebsen* can quickly find an optimal sensing path even if LoS is blocked or misaligned. On average, *Trebsen* achieves convergence to the optimal result within 10 steps. Compared with random search, *Trebsen* exhibits a 90% increase in search speed. In specific applications, experimental results show that *Trebsen* significantly enhances heartbeat sensing performance in scenes with occluded or misaligned LoS. Compared to non-beamforming, *Trebsen* demonstrates a reduction of 23.6% in average HR error and 27.47% in average IBI error, respectively.

2 RELATED WORK

2.1 MmWave-based sensing

Wireless fine-grained sensing based on mmWave radar has attracted extensive attention from researchers. As people pay more attention to their own health, the sensing based on vital signs has attracted the attention of academia and industry, such as respiration and heartbeat signal [18, 33, 35], blood pressure measurement [27], body temperature monitoring [9] etc. Xu et al. [33] proposed a non-contact high-definition heart monitoring system, which can provide a full spectrum of Electrocardiogram (ECG)-like heart activities. Shi et al. [27] proposed a contact-free mmWave-based blood pressure (BP) measurement system, which uses the Delay-Doppler domain feature transformation method to exploit mmWave signal features to improve signal quality. In addition, mmWave radar has found widespread applications in security and privacy-related fields due to its unique characteristics and capabilities, such as detection [6, 36], recognition[12, 38], authentication [34], eavesdropping[13, 29], etc.

Xu et al. [34] exploit the penetrability, material sensitivity, and fine-grained sensing capability of mmWave to build an anti-spoofing mmFace system, which allows mmFace to achieve reliable liveness detection and face authentication. Liu et al. [23] proposed a first noise-resistant multi-modal speech recognition system that fuses two distinct voice sensing modalities, i.e., mmWave signals and audio signals from a microphone, together. Due to the inherent correlation and complementarity between different modalities, the fine-grained target perception of multi-modal fusion, e.g., microphone [23], IMU [24] and camera [8], based on mmWave has also attracted the attention of researchers. However, these methods are tailored to specific application scenarios to improve the performance of fine-grained motion sensing at the back-end signal processing level.

2.2 MmWave-based beamforming

Various beamforming techniques are spatial filtering methods widely used in wireless communication [37] and sonar [15] applications. Beamforming technology has a wide range of applications in the communications field, and there are many types, including analog beamforming [37], and digital beamforming [5]. Transmitter beamforming usually uses analog components, e.g., phase shifters, to focus the beam of a transmitting antenna array in a specific direction [37]. While receiver beamforming usually uses digital processing techniques to optimize the reception of signals in a specific direction[5]. However, whether these beamforming technologies are designed through hardware or software algorithms, their primary purpose is to improve communication signal quality, thereby ensuring communication performance stability. Moreover, the existing hybrid beamforming methods employ a combination of analog beamformers in the radio frequency (RF) domain, along with digital beamforming in the baseband, connected to the RF using a smaller number of up/down conversion chains [25]. For instance, in the transmitter, a baseband digital beamformer pre-coders data streams to outputs, which are then upconverted to RF and mapped via an analog beamformer to antenna elements for transmission [17]. However, these methods ensure the reduction of communication costs and the enhancement of communication stability by designing specific hardware and signal precoders, which may not be easily generalized for fine-grained motion perception. In recent years, with the development of sensory integration, mmWave beamforming technology has gained widespread attention in sensing applications [32, 36]. For example, Wu et al. [32] significantly improve the spatial resolution by performing digital beamforming overall receive antennas. However, previous methods predominantly concentrate on either consider transmitter beamforming [37] or receiver beamforming [5, 32]. Notably, there is a lack of comprehensive investigations into the collaborative beamforming involving both the transmitter and receiver. Therefore, in this paper, we propose a novel scheme for fine-grained motion sensing utilizing a hybrid beamforming method in collaboration between the transmitter and receiver of a mmWave radar system.

3 EMPIRICAL STUDY

In this section, we explore factors that influence fine-grained motion sensing based on mmWave radar. We first define the motion vector as the motion direction of a fine-grained motion target. The incident angle refers to the angle between the mmWave incident signal based on TxBF and motion vector, and the reflection angle refers to the angle between the mmWave received signal based on RxBF and motion vector. Specifically, we examine the impact of the incident angle and reflection angle, which is the angle between the mmWave incident or reflected signal and motion vector. Additionally, we study the effects of propagation paths and reflection coefficients of walls on the sensing of fine-grained motion.

3.1 The Influence of Incident and Reflection Angle on Fine-Grained Motion

Observation 1: *As the incident or reflection angle of a signal varies from* 0 *to* 90°*, the signal energy strength and phase variation can decrease exponentially.*

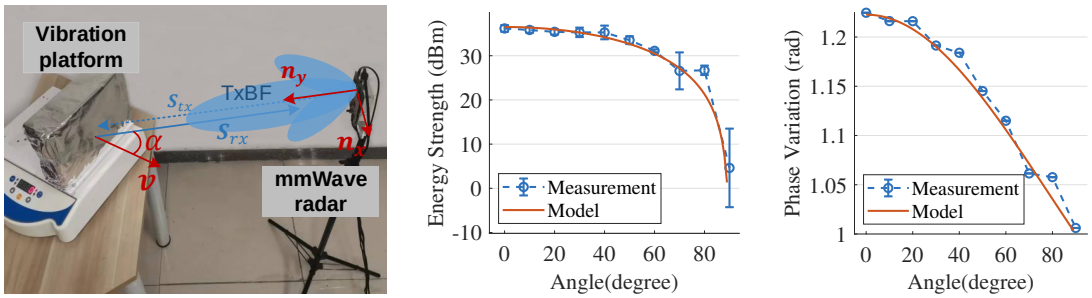

(a) Experiment setup (b) Received signal strength (c) Received phase variation

Fig. 2. Impact of incident angle α on perception performance based on transmitter beamforming

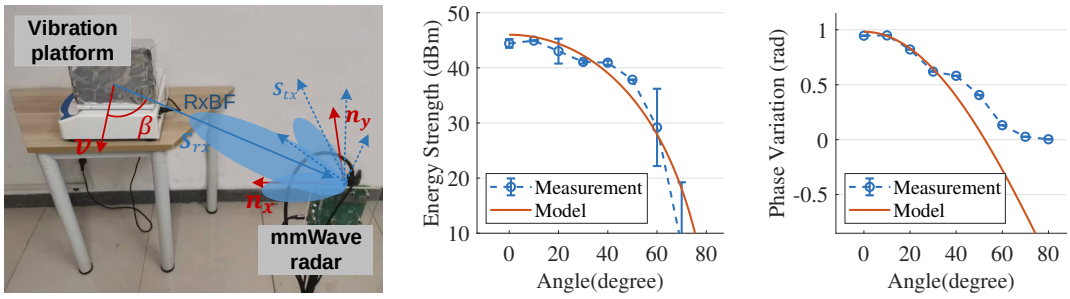

(a) Experiment setup (b) Received signal strength (c) Received phase variation

Fig. 3. Impact of received angle β on perception performance based on receiver beamforming.

The key idea of Transmitter Beamforming (TxBF) is to transmit a signal via antenna array simultaneously and coherently to achieve a higher gain in the main focused field of view. As shown in Fig.2(a), we define the motion vector $\boldsymbol{v}$ as the motion direction of the vibration platform, and the incident angle α refers to the angle between the mmWave incident signal based on TxBF and motion vector $\boldsymbol{v}$. To explore the influence of the incident angle on the fine-grained motion-sensing performance, we design experiments to study the impact of reflected signal strength and phase variation as the incident angle changes. Specifically, we use a vibration platform to generate fine-grained motion. We use TI's AWR6843-ISK [1] mmWave radar to perceive the motion state. The vibration platform is located directly in front of the mmWave radar, the distance between the platform and the mmWave radar is set to $1.2m$, and the transmitting angle ϕ of beamforming is set to 0, as shown in Fig.2(a). To ensure the effectiveness and accuracy of experiments, we use beamforming to transmit Frequency Modulated Continuous Wave (FMCW) signals at the transmitter and omnidirectional reception at the receiver to obtain target motion signals. To study the relationship between the incident angle and the perceived signal, as the incident angle varies from 0 to 90°, we analyze the power and phase of the reflected signal. Fig.2(b) shows that the signal strength exponentially increases sharply with increasing incident angle. Fig.2(c) shows that the theoretical phase variation function $\exp[j\frac{2\pi}{\lambda}\frac{\mathbf{v}}{\|\mathbf{v}\|}cos(\alpha)]$ with respect to the incident angle agrees well with the measured result. With the emergence of Multiple-Input-Multiple-Output (MIMO) technology, receiver beamforming (RxBF) has gained significant attention in the field of wireless communication and sensing. So, how does RxBF affect the perceived signal? As shown in Fig.3(a), the reflection angle α refers to the angle between the mmWave received signal based on RxBF and motion vector $\boldsymbol{v}$. Specifically, to study the relationship between the reflection angle β and the received signal S_{rx}, we transmit signals omnidirectionally at the transmitter and use RxBF directional reception

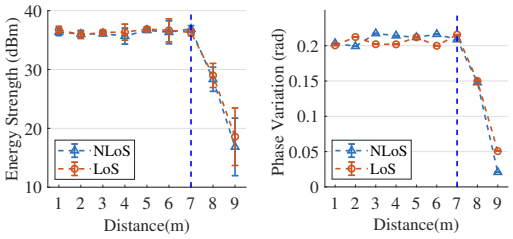

(a) Energy strength (b) Phase variation

Fig. 4. The influence of propagation distance on sensing performance in LoS and NLoS propagation paths.

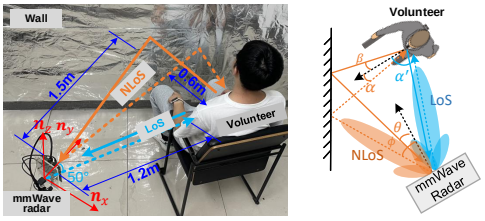

(a) Experiment setup. (b) Positional relationship map.

Fig. 5. Experimental deployment and location relationship.

at the receiver. The reflection angle β varies from 0 to 90° by changing the position of the vibration platform. Fig.3(b) shows that the signal strength exponentially increases sharply with increasing reflection angle. Fig.3(c) shows that the theoretical phase variation $\exp[j\frac{2\pi}{\lambda}\frac{\mathbf{v}}{\|\mathbf{v}\|}cos(\beta)]$ with respect to the reflection angle agrees well with the measured result. Therefore, we can use TxBF and RxBF to minimize the incident and reflection angle, thereby increasing the signal energy strength and angle variation of the fine-grained motion signal.

3.2 The Influence of Signal Propagation Distance on Fine-Grained Motion

Observation 2: *Whether it is LoS or NLoS, the signal propagation attenuation with distance remains stable within a certain sensing distance but increases significantly after exceeding a certain threshold.*

In traditional scenarios with LoS propagation, the LoS path is often regarded as the optimal signal propagation path, due to its direct and unobstructed path between the radar and target. However, the propagation path of LoS does not always exist in the scene. Considering the reflection and diffraction effects of wireless signals, the NLoS reflection or diffraction around obstacles can be used to sense target signals. Hence, how can we obtain higher-quality motion signals when LoS is obstructed or misaligned? To tackle this issue, we compare the effect of signal propagation distance on the perceived signal energy and target motion state in LoS and NLoS paths. Specifically, we design experiments to study the relationship between the propagation distance and the received signal in NLoS and LoS scenarios. For the experiment setup of LoS propagation distance attenuation, the vibration platform is located directly in front of the mmWave radar, and the incident angle is set to 0. To reduce the impact of reflective surfaces, we set up metal walls as reflective surfaces. We define the signal coverage distance as the maximum distance at which the radar signal can propagate without being completely blocked by obstacles. The maximum signal coverage distance of the mmWave radar is set to $9.6m$, and the measurement distance from mmWave radar to the target varies from $1m$ to $9m$. Moreover, we construct a primary reflection path for the experimental setup of NLoS propagation distance attenuation to satisfy the signal propagation distance from $1m$ to $9m$. As shown in Fig.4(a) and Fig.4(b), we notice that whether it is LoS or NLoS propagation path, the propagation distance attenuation [14] is almost unchanged within distance $7m$. However, when the distance exceeds $7m$, the signal energy strength and phase variation decrease sharply as the signal propagation distance increases, resulting in the sensing performance dropping sharply.

3.3 The Influence of Signal Propagation Paths on Fine-Grained Motion

Observation 3: *The perception signal quality based on NLoS paths is better than LoS in some scenarios.*

We know that the signal propagation distance attenuation remains constant within a certain propagation distance. To study the influence of LoS and NLoS propagation paths on the sensing performance, we design comparative experiments, using mmWave radar to perceive the user's breathing and heartbeat signals on the LoS

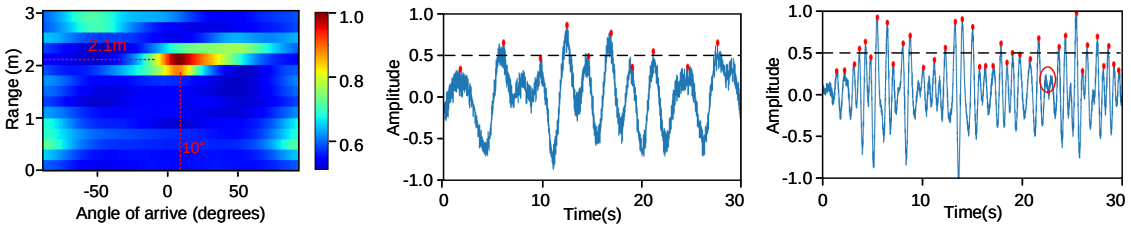

(a) Range angle heatmap (b) Respiratory estimation is 20 bpm (Ground truth 21 bpm) (c) Heartbeat estimation is 72 bpm(Ground truth is 73 bpm)

Fig. 6. TxBF-based vital signs (i.e., respiratory, heartbeat) sensing in NLoS scenarios.

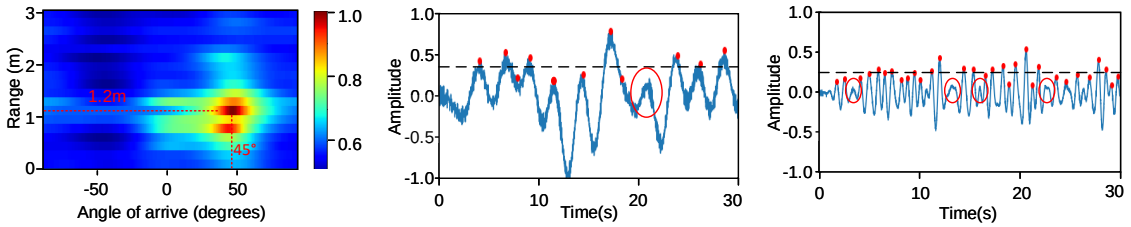

(a) Range angle heatmap (b) Respiratory estimation is 18 bpm (Ground truth is 21 bpm) (c) Heartbeat estimation is 62 bpm (Ground truth is 73 bpm)

Fig. 7. TxBF-based vital signs (i.e., respiratory, heartbeat) sensing in LoS scenarios.

and NLoS paths, respectively. Specifically, to maintain the consistency of the experimental setup, we perceive the respiratory and heartbeat signals of the LoS and NLoS propagation paths separately under the same deployment, as shown in Fig.5. We use TxBF to transmit FMCW signals to LoS and NLoS path and obtain omnidirectional reflected signals, respectively, as shown in Fig.6 and Fig.7. As shown in Fig.6(a) and Fig.7(a), we can estimate the location of the volunteers at $2.1m$ and $1.2m$ in the NLoS and LoS paths, respectively. To study the sensing performance of breathing and heartbeat signals in NLoS and LoS path scenes, we compare Fig.6(b) and Fig.7(b), and find that the error rate of respiration rate per minute estimated based on LoS is about 14.3%, while the error rate of respiration rate per minute based on NLoS is about 4.7%. Comparing Fig.6(c) and Fig.7(c), the estimation error rate of heartbeat rate based on LoS is about 15.1%, while the estimation error rate of heartbeat rate based on NLoS is about 1.4%. Therefore, constructing an NLoS path becomes a viable approach to obtaining higher-quality sensing signals in scenarios where the LoS propagation path is obstructed or misaligned.

4 SENSING MODEL BASED ON HYBRID BEAMFORMING.

The essence of mmWave-based sensing is to perceive the target motion, such as chest motion for respiration monitoring, finger motion for gesture recognition, etc. Due to the short wavelength, mmWave sensing is easily interfered with by environmental noise and multipath effects, which poses a great challenge to accurately sensing fine-grained target movements, such as the movement of vocal cords in eavesdropping. Generally, the received signals are fused signals from the two paths of LoS and NLoS. As shown in Fig. 8, it is the basic model of fine-grained motion sensing based on mmWave radar. Therefore, to study the factors that affect the performance of mmWave sensing of fine-grained motion, we analyze the signal channel coefficients in the sensing process to provide theoretical support for how to reduce signal channel attenuation in the *Trebsen*.

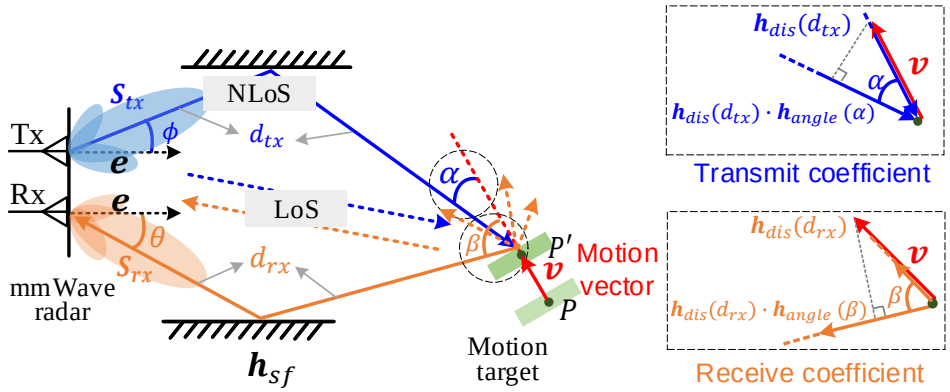

Fig. 8. Hybrid beamforming based on transmitter-receiver collaboration for fine-grained motion-sensing modeling. (A detailed exploration of the modeling approach that leverages collaborative efforts between the transmitter and receiver for achieving fine-grained motion sensing.)

4.1 Signal Channel Coefficient from Radar to Target

The short wavelength leads to a weakened diffraction effect, which makes the mmWave signal highly directional. We first define the motion vector as the motion direction of a fine-grained motion target. The angle between the incident direction of the mmWave signal and the motion vector $\mathbf{v}$ of the target is defined as incident angle α. According to 3.1, the incidence angle can affect received signal quality. Specifically, if the incident angle α is 0°, the motion of the moving target makes the phase of the incident signal change to the greatest extent. Therefore, given the incident angle α, the signal of the incident signal in the direction of the motion vector can be expressed as:

$$h_{tx} = h_{dis}(d_{tx}) \cdot h_{angle}(\alpha), \tag{1}$$

where d_{tx} is the propagation distance from the transmitter to the target, and $h_{angle}(\alpha)$ is the channel coefficient caused by incident angle, which denotes the projected component of the incident signal in the direction of the motion vector, it can be expressed as[22, 30]:

$$h_{angle}(\alpha) = \sigma_\alpha cos(\alpha) \cdot \exp[j\frac{2\pi}{\lambda}\frac{\mathbf{v}}{\|\mathbf{v}\|}cos(\alpha)], \tag{2}$$

where $\sigma_\alpha cos(\alpha)$ represents energy coefficient caused by incident angle, σ_α is the incident signal energy factor.

Similarly, the relationship between the reflected signal and reflection angle can be expressed as:

$$h_{rx} = h_{dis}(d_{rx}) \cdot h_{angle}(\beta), \tag{3}$$

where d_{rx} is the propagation distance from the target to the receiver, and $\mathbf{h}_{angle}(\beta)$ is the channel coefficient caused by reflection angle, which denotes the projected component of the reflection signal in the direction of the motion displacement vector, can be expressed as:

$$h_{angle}(\beta) = \sigma_\beta cos(\beta) \cdot \exp[j\frac{2\pi}{\lambda}\frac{\mathbf{v}}{\|\mathbf{v}\|}cos(\beta)], \tag{4}$$

where $\sigma_\beta cos(\beta)$ represents energy coefficient caused by reflection angle, σ_β is the reflected signal energy factor.

Furthermore, considering that the propagation distance coefficient $h_{dis}(d)$ of the signal is inevitable and related to the propagation distance, it can be expressed as [14]:

$$h_{dis}(d) = \frac{\lambda\sqrt{G}}{4\pi d}\exp(j\frac{2\pi d}{\lambda}), \tag{5}$$

where the factor $(\lambda/4\pi d)$ is called the free-space loss factor, G is the gain of transmitter, d is the propagation distance from transmitter to target, λ is the signal wavelength. We consider signal channel coefficients caused by reflective surfaces, the complex reflection surface attenuation $\mathbf{h}_{sf}$ of the reflective surface [7].

4.2 Signal Channel Coefficient of Motion State

Considering that the most concerning thing in sensing applications is the motion state of the sensing target. Changes in the motion state of the target cause changes in the phase and energy of the reflected signal. To analyze the signal channel coefficient caused by motion, assuming that the incident angle of the signal is 0°. The signal channel coefficient $\mathbf{h}_v$ caused by target motion can be expressed as:

$$h_v = \sigma_v \exp(j\frac{4\pi}{\lambda}\|\mathbf{v}\|), \tag{6}$$

where σ_v is the energy coefficient caused by the target, $\mathbf{v}$ is the motion displacement vector of the target.

4.3 Analysis of Signal Channels

We find that the received signal contains dynamically adjustable components H, i.e., incident angle coefficient $h_{angle}(\alpha)$, reflection angle coefficient $h_{angle}(\beta)$ and multipath reflective surface coefficient h_{sf}, and static non-adjustable components, i.e., the transmitted signal S_{tx}, the motion state coefficient h_v. Therefore, the received signals can be expressed as:

$$S_{rx} = S_{tx}h_v \cdot \underbrace{h_{dis}(d)h_{angle}(\alpha)h_{angle}(\beta)h_{sf}}_{H}, \tag{7}$$

In particular, there is no reflective surface coefficient h_{sf} in the LoS perception path, so we can consider it to be a constant 1.

Considering that signal propagation usually consists of one LoS channel and m NLoS sensing channels between the target and the transceiver, according to Eq.7, the received signals caused by multi-propagation channels can be expressed as:

$$S_{rx\_multi} = S_{tx}h_v \cdot [w_0 H_{los} + \sum_{i=1}^{m} w_i H_{nlos}(i)], \tag{8}$$

where H_{los} and $H_{nlos}(i)$ represent the dynamically adjustable components of the received signal in the LoS and NLoS path, respectively. In an ideal scenario, S_{rx_multi} should be capable of receiving all signals. However, if some channels become blocked or experience attenuation, it will lead to a significant reduction in the received signal S_{rx_multi}. To maximize the received signal S_{rx_multi}, we desire the primary signal component to propagate along the path with minimal channel attenuation. Due to its high directivity, mmWave-based beamforming enables the primary signal component to be directed along a specific path, thereby maximizing the received signal. Therefore, to reduce the additional channel attenuation, we propose employing a hybrid beamforming configuration to concentrate the total energy onto the primary channels. Specifically, we use hybrid beamforming based on transmitter-receiver collaboration to obtain the parameters $w_i,\ i = 0, ...m$.

4.4 Hybrid Beamforming

The goal of hybrid beamforming is to select an optimal channel to maximize the received signal. Assume that an array antenna comprising n_t transmitting antennas and n_r receiving antennas, each transmitting antenna and receiving antenna are isomorphic and uniformly, the transmitting signal vector and receiving signal vector are $\mathbf{s}_{tx}$ and $\mathbf{s}_{rx}$, respectively. As shown in Fig.8, given a signal transmitting angle ϕ or receiver angle θ, which denotes the angle between the signal propagation path and the normal-vector $\mathbf{e}$ of the antenna plane. The signal

beamforming by the transmitter or receiver and directed towards ϕ can be expressed as:

$$\begin{aligned} S_{txbf}(\phi) &= \mathbf{s}_{tx} \cdot \mathbf{a}^T(\phi), \\ \mathbf{a}(\phi) &= [1, e^{j\frac{2\pi d_t}{\lambda} sin(\phi)}, ..., e^{j(n_{t/r}-1)d_t \frac{2\pi}{\lambda} sin(\phi)}]. \end{aligned} \tag{9}$$

Where $\mathbf{a}(\phi)$ is the steering vector of transmitter and receiver antennas, respectively. According to Eq.(7), each receiving antenna signal S_{rx} based on transmitter beamforming is expressed as:

$$S_{rx} = \mathbf{s}_{tx} \cdot \mathbf{a}_{tx}^T(\phi) h_v h_{dis}(d) h_{angle}(\alpha) h_{angle}(\beta) h_{sf}. \tag{10}$$

The receiving signal vector composed of all antennas is $\mathbf{s}_{rx} = [S_{rx}^1, S_{rx}^1, ...S_{rx}^{n_r}]$, the hybrid beamforming signal S_{rx_hbf} is expressed as:

$$S_{rx\_hbf} = \mathbf{s}_{rx} \cdot \mathbf{a}_{rx}^T(\theta). \tag{11}$$

We can change the signal propagation path by adjusting the steering vector $\mathbf{a}_{tx}^T(\phi)$ and $\mathbf{a}_{rx}^T(\theta)$, to change the signal incident angle and reflection angle, that is, α, β. Therefore, we can solve the steering vector under the optimal propagation channel by maximizing the hybrid beamforming received signal S_{rx_hbf}.

4.5 Hybrid Beamforming Parameters Optimization

The component $\mathbf{h}_{dis}$ and $\mathbf{h}_{sf}$ primarily comprises energy attenuation due to the propagation path between the target and the transceiver. Meanwhile, the incident angle α and reflection angle β directly influence the sensing performance of the target's motion sensing. Therefore, the propagation path attenuation $\mathbf{h}_{dis}$ must satisfy the maximum path attenuation constraint that can perceive the target. Considering that the signal transmitting angle ϕ and signal reception angle θ based on hybrid beamforming in NLoS can change the incident angle α and reflection angle β. Our goal is to estimate an optimal propagation path attenuation $w_i H(i)$, by fine-tuning the signal transmitting angle ϕ and signal reception angle θ of hybrid beamforming configuration, as detailed in Sec.4.4. To fine-tune the transmitting angle ϕ and reception angle θ for maximizing the received signal, we can derive the optimization function using Eq.(11) as:

$$\begin{aligned} \underset{\phi,\theta}{argmax}\ S_{rx\_hbf} &= \underset{\phi,\theta}{argmax} \sum_{j=0}^{n_r-1} \sum_{i=0}^{n_t-1} S_{tx}^{\langle i,j \rangle} \mathbf{a}_{tx}^i(\phi) h_{dis}^{\langle i,j \rangle}(d) h_{angle}^{\langle i,j \rangle}(\alpha) h_{angle}^{\langle i,j \rangle}(\beta) h_{sf}^{\langle i,j \rangle} \mathbf{a}_{rx}^j(\theta), \\ s.t. &\begin{cases} h_{dis}(d) h_{sf} > T_1, \\ h_{angle}(\alpha) h_{angle}(\beta) < T_2, \\ \phi, \theta \in \{-60, -59, ...60\}, \end{cases} \end{aligned} \tag{12}$$

where $S_{tx}^{\langle i,j \rangle}$ is the transmitting signal from *i-th* transmitter antenna to *j-th* receiver antenna, $h_{dis}^{\langle i,j \rangle}(d) h_{sf}^{\langle i,j \rangle}$ is carrier signal attenuation relative to the propagation distance and reflecting surface in $\langle i, j \rangle$ propagation channel, T_1 is the minimum channel coefficient, $h_{angle}^{\langle i,j \rangle}(\alpha) h_{angle}^{\langle i,j \rangle}(\beta)$ is sensing angle attenuation relative to the incident angel α and reception angle β, T_2 in $\langle i, j \rangle$ propagation channel.

5 QUANTIFYING PERCEPTUAL SIGNAL QUALITY

Our goal is to enhance the perceived signal quality by optimizing the steering vector in Eq.12, so that the primary component of the sensing signal along the channel with minimal propagation attenuation. Hence, it is crucial to establish an effective metric for assessing the quality of the sensing signal to search for an optimal motion sensing signal. To tackle this issue, we use Carrier-Energy-to-Noise Ratio (*CENR*), which is associated with the perceived target's position and its motion status (i.e., static or dynamic), and Baseband Entroy ($Entroy_{bs}$), which is directly related to the quality of the target's fine-grained motion signal, to evaluate the signal quality.

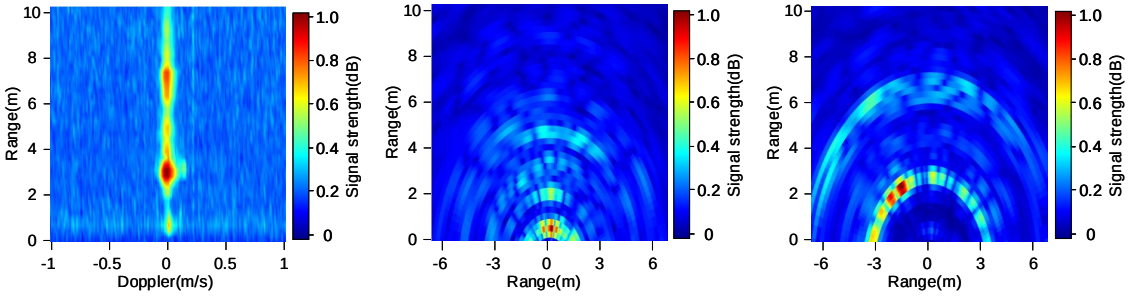

(a) The Range-Doppler heatmap is obtained when the angle dimension is set to 0°.

(b) The Range-Angle heatmap is obtained by averaging the Doppler dimension.

(c) The Range-Angle heatmap is obtained by maximizing the Doppler dimension.

Fig. 9. Carrier SINR: This metric jointly evaluates the carrier signal quality by generating a heatmap from the Range-Doppler heatmap and a spatial heatmap from the Range-Angle perspective.

5.1 Carrier-Energy-to-Noise Ratio

The conventional approach to assessing fine-grained moving targets typically relies on considering the range and Doppler velocity to estimate the range bin where the target is positioned. Nevertheless, our research has revealed that considering the target's direction is equally imperative for ensuring the high quality of the perceived signal, as discussed in Section 3.1. To provide a comprehensive estimation of the *CENR*, we introduce two components, $CENR_{RD}$ and $CENR_{RA}$, which are derived from the Range-Doppler heatmap (as shown in Fig.9(a)) and Range-Angle static heatmap (as shown in Fig.9(b)), respectively. The noise floor and signal power can be obtained using the two-dimensional constant-false-alarm-rate (CFAR) [19] method based on RD heatmap and RA heatmap. The *Carrier Energy* is defined as the intersection of these two components and can be expressed as:

$$\begin{aligned} CENR^{\langle i,j,k\rangle}(t) &= CENR_{RD}^{\langle i,j\rangle}(r,d,t) \cap CENR_{RA}^{\langle i,k\rangle}(r,a,t) \\ &= \frac{\boldsymbol{P}_{obj}^{\langle i,j\rangle}(r,d,t)}{\boldsymbol{P}_{noise}(r,d,t)+\boldsymbol{P}_{inf}(r,d,t)} \cap \frac{\boldsymbol{P}_{obj}^{\langle i,k\rangle}(r,a,t)}{\boldsymbol{P}_{noise}(r,a,t)+\boldsymbol{P}_{inf}(r,a,t)}, \end{aligned} \tag{13}$$

where i, j, and k represent the Range, Doppler, and Angle bins, respectively. $\boldsymbol{P}_{obj}^{\langle i,j\rangle}(r,d,t)$, $\boldsymbol{P}_{noise}(r,d,t)$ and $\boldsymbol{P}_{inf}(r,d,t)$ represent the target signal power, noise power, and interference signal power in the Range-Doppler heatmap, respectively. As depicted in Fig.9(c), we introduce a Range-Doppler-Angle (RDA) signature obtained by amalgamating information from both the Range-Doppler (RD) and Range-Angle (RA) heatmaps. Hence, the *CENR* can be expressed as:

$$CENR^{\langle i,j,k\rangle}(t) = \frac{|S_{rx}^{obj}(r_i,d_j,a_k,t)|^2}{|S_{rx}^{noise}(r,d,a,t)|^2+\sum_m |S_{rx}^{inf}(r,d,a,t)|^2}. \tag{14}$$

Here, $|S_{rx}^{noise}(r,d,a,t)|^2$ is noise power and easily obtained using the CFAR method. $|S_{rx}^{obj}(r_i,d_j,a_k,t)|^2$ is the target power. The maximum value exceeding the noise floor is used as the target power, and its corresponding $\langle i,j,k\rangle$ is the target location candidate. $\sum_m |S_{rx}(r,d,a,t)|^2$ is interference power. Considering single target detection, other target positions beyond the noise floor are considered interference targets.

5.2 Baseband Entropy

It is evident that *CENR* does not precisely quantify the quality of fine-grained motion signals in Section 5.1. To address this limitation, we propose a *baseband entropy* as a more precise metric for assessing the quality of

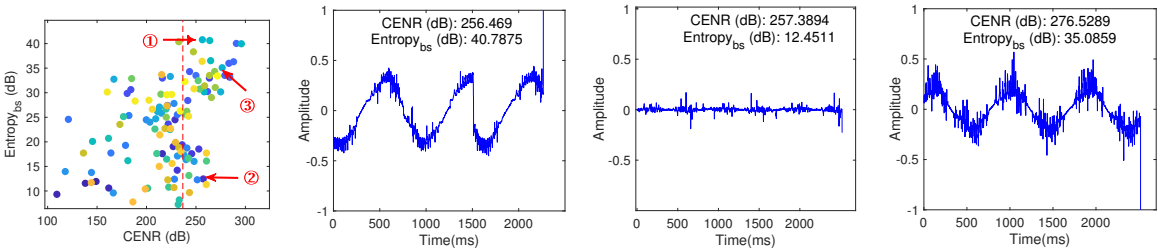

(a) Two-dimensional *PSINR*. (b) Phase signal of case 1. (c) Phase signal of case 2. (d) Phase signal of case 3.

Fig. 10. The example of effectiveness analysis based on two-dimensional *PSINR* metric. (Case 1 is the phase signal in low *CENR* and high $Entropy_{bs}$, case 2 is the phase signal in low *CENR* and low $Entropy_{bs}$, and case 3 is the phase signal in high *CENR* and high $Entropy_{bs}$.)

fine-grained motion signals. According to the information provided in Section 5.1, if the $CENR^{\langle i,j,k\rangle}$ exceeds the threshold T_{cs}, then the bin with coordinates $\langle i, j, k\rangle$ is considered a potential target location. We can extract the phase signals from candidate positions $\langle i, j, k\rangle$ in consecutive N frames and splice them:

$$y^{\langle i,j,k\rangle} = \sum_{t=1}^{N} Phase\{S_{obj}^{\langle i,j,k\rangle}(t)\}, \tag{15}$$

where $Phase\{\cdot\}$ represents the phase extraction operation of complex signals. The extraction methods of motion signals are different for different sensing applications. Therefore, in order to quantify the fine-grained motion signal quality under different applications, we propose *baseband entropy* to quantify the signal quality of fine-grained sensing.

$$Entropy_{bs}^{\langle i,j,k\rangle}(t) = \frac{|\mathcal{F}(y^{\langle i,j,k\rangle})|^2}{|y_{noise}|^2 + |y_{inf}|^2}, \tag{16}$$

where, $\mathcal{F}(\cdot)$ represents that feature extraction operations in different application scenarios. Assuming that we know the frequency range of the sensed motion, according to Parseval's Theorem, we can obtain the power of the target motion frequency by performing FFT on the characteristic signal $\mathcal{F}(y)$. For example, in breathing and heartbeat sensing scenarios, the symbol $\mathcal{F}(\cdot)$ denotes a combination of differential and band-pass filtering operations applied to phase signals. In lip recognition applications, $\mathcal{F}(\cdot)$ encompasses a series of operations, including low-pass filtering, downsampling, and micro-doppler [10] feature extraction.

5.3 Effectiveness Analysis of *PSINR*

According to the above analysis, *PSINR* can be expressed as:

$$PSINR^{\langle i,j,k\rangle} = \begin{cases} (Entropy_{bs}^{\langle i,j,k\rangle}, CENR^{\langle i,j,k\rangle}) & \text{if } CENR^{\langle i,j,k\rangle} \geq T_{cs} \\ (0, CENR^{\langle i,j,k\rangle}) & others. \end{cases} \tag{17}$$

To establish the efficacy of the *PSINR* metric, we conducted specific experiments to assess the quantitative performance and stability of this indicator. The experimental setting is similar to Section 3.1. We use transmit beamforming (TxBF) to scan the front of the radar in the positive and negative 60° directions and use *PSINR* to calculate the signal quality at the receiver. As shown in Fig. 10(a), it is the relationship between *CENR* and $Entropy_{bs}$, it can be seen that as *CENR* increases, $Entropy_{bs}$ also shows an upward trend. Specifically, upon comparing Fig. 10(b) and 10(c), it becomes evident that, under identical *CENR* conditions, higher $Entropy_{bs}$ values correspond to the superior quality of the fine-grained motion signal. In contrast, when comparing Fig. 10(b) and 10(d), it is apparent that *CENR* does not adequately represent the quality of the fine-grained motion signal.

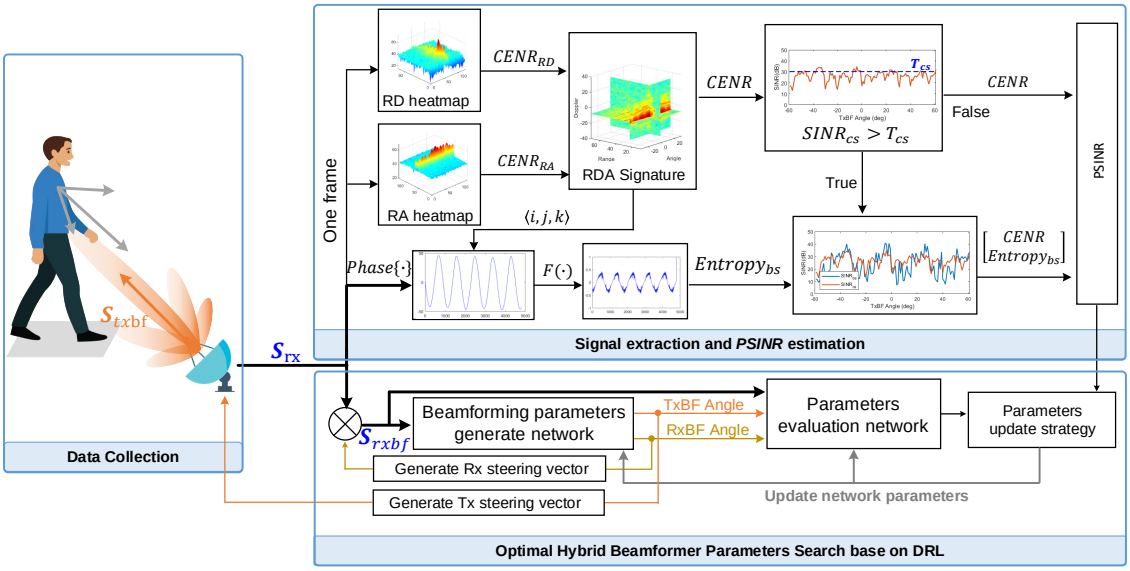

Fig. 11. System architecture of hybrid beamforming based on transmitter-receiver collaboration.

When $CENR$ exceeds the threshold T_{cs}, $Entropy_{bs}$ proves to be a more accurate metric for assessing the quality of fine-grained signals. To determine the threshold of $CENR$ for a scene, we initially employ an omnidirectional antenna configuration to obtain the $CENR$ in the current scene (e.g., Fig.9). According to Eq.(14), we derive the maximum $CENR_{max}$ and minimum $CENR_{min}$ of the current scene as a reference value, where the value can be expressed as $CENR_{max} = \max(CENR^{\langle i,j,k \rangle}(t))$, $CENR_{min} = \min(CENR^{\langle i,j,k \rangle}(t))$. As shown in Fig.9, to enhance the robustness of $CENR$ and consider the varying reflected signal strengths from different materials, we introduce a normalization step, i.e., $CENR_{norm} = (CENR - CENR_{min})/(CENR_{max} - CENR_{min})$. Therefore, we can set the carrier signal strength threshold T_{cs} to $0.8 * CENR_{norm}$ in the current scene.

6 SYSTEM DESIGN

We propose a novel *Trebsen*, a Transmitter-REceiver collaboration-based Beamforming scheme SENsing using commercial mmWave radars, to improve the perception signal quality efficiently. As shown in Fig.11, the system framework consists of the following two modules: 1) signal extraction and *PSINR* calculation based on mmWave radar, and 2) optimal hybrid beamformer parameters search based on deep reinforcement learning (DRL).

6.1 Signal Extraction and *PSINR* Calculation based on MmWave Radar

To achieve an accurate estimation of *PSINR*, the initial step involves determining both the target's location and its $CENR$. The $CENR$ can be obtained through calculating $SINR_{RD}$ and $SINR_{RA}$, as outlined in Eq. (13) detailed in Section 5.1. As shown in Fig. 9(a), the range-doppler heatmap is obtained by performing FFT operations on the intermediate frequency (IF) signal in the fast window and the slow window, respectively. Accordingly, as shown in Fig. 9(b), the range-angle heatmap is obtained by performing FFT operations on the IF signal in a fast window and different antennas, respectively. Based on Eq. (14), we can ascertain the target range, doppler, and angle bins $\langle i, j, k \rangle$ by computing the maximum $CENR$.

To assess the quality of the motion signal at the target location, we gather the phase signals from candidate positions $\langle i, j, k \rangle$ in consecutive sets of N frames and concatenate them, according to Eq.(15). Due to limitations imposed by hardware, the initial phase randomness of each frame signal gives rise to a phase discontinuity

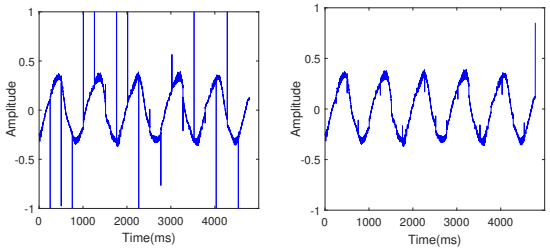

(a) Before phase compensation. (b) After phase compensation.

Fig. 12. Fine-grained motion phase signal before and after phase compensation.

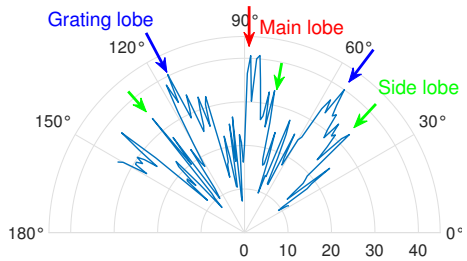

Fig. 13. The beamforming pattern based on the *PSINR* metric when *CENR* is fixed.

between two adjacent frames, as illustrated in Fig. 12(a). To solve this problem, we propose an adjacent frame phase calibration method. Specifically, by calculating the phase gap of adjacent frames and then compensating the phase of subsequent frames, the compensated phase signal is obtained, as shown in Fig. 12(b).

After obtaining the phase information, use the operation $\mathcal{F}(\cdot)$ to extract the object signal feature for different application scenarios, according to Eq.(16). Is it feasible to exclusively employ the TxBF detection method and utilize *PSINR* as the assessment metric for ascertaining the optimal signal propagation path? We use TxBF to scan $[-60°, +60°]$ with a step size of 1°, and use Eq. 17 to calculate the signal quality under its corresponding path, as shown in Fig. 13. It's important to highlight that the *PSINR* outcome exhibits not just a single anticipated peak, but rather multiple peaks that cannot be differentiated. Assuming that the antennas phase shift is $\Delta\phi$, the beam angle θ can be expressed as [11]:

$$\theta = \arcsin\left(\frac{m \times 2\pi + \Delta\Phi}{2\pi} \times \frac{\lambda}{d}\right), \text{where } m = 0, \pm1, \pm2... \tag{18}$$

where λ is the wavelength, d is the space between its antennas. Since existing commercial mmWave radars are designed for MIMO applications and their antenna spacing $d > \lambda$, the θ is not unique in the Eq.(18). Specifically, the space $d = 2\lambda$ of our hardware, when the expectation of TxBF beam angle is 0°, the antenna phase shift $\Delta\phi$ is 0°, the Eq.(18) will have three real solutions, i.e., $m = 0$ and $m = \pm1$. Therefore, the real TxBF beam angle is 0°, and the ±30° is the grating lobe, as shown in Fig.13. To address the issue of *PSINR* peak ambiguity caused by the grating lobe in software, we propose employing receiver beamforming (RxBF) to implement spatial filtering at the receiver, thereby enhancing signals in specific directions. Given the possibility of a blocked or misaligned LoS path, setting the RxBF beam angle equal to the TxBF beam angle might not be the most effective solution for obtaining the maximum *PSINR* signals. Therefore, we need a more feasible method to estimate the RxBF beam angle, and maximum the *PSINR* of signal even in scenarios where the LoS is blocked or misaligned.

6.2 Optimal Hybrid Beamformer Parameters Search base on DRL

In order to ensure that the primary sensing signal propagates along the minimum signal attenuation path, a common method is to use an enumeration or random search method. Considering the vast search space of the optimization problem described in Eq.(12) and the stochastic nature of the objective, finding the optimal beamforming parameters in a limited time is challenging, whether using enumeration or dichotomy methods. Fortunately, the recent advances in machine learning provide us with an opportunity to address this challenge. Therefore, to obtain the TxBF and RxBF parameters, ϕ and θ, to make the primary sensing signal propagate along the minimum signal attenuation path, we propose deep reinforcement learning (DRL) to solve the parameters of the beamformer, as shown in Fig.14. This method contains two aspects: 1) The hybrid beamforming parameters

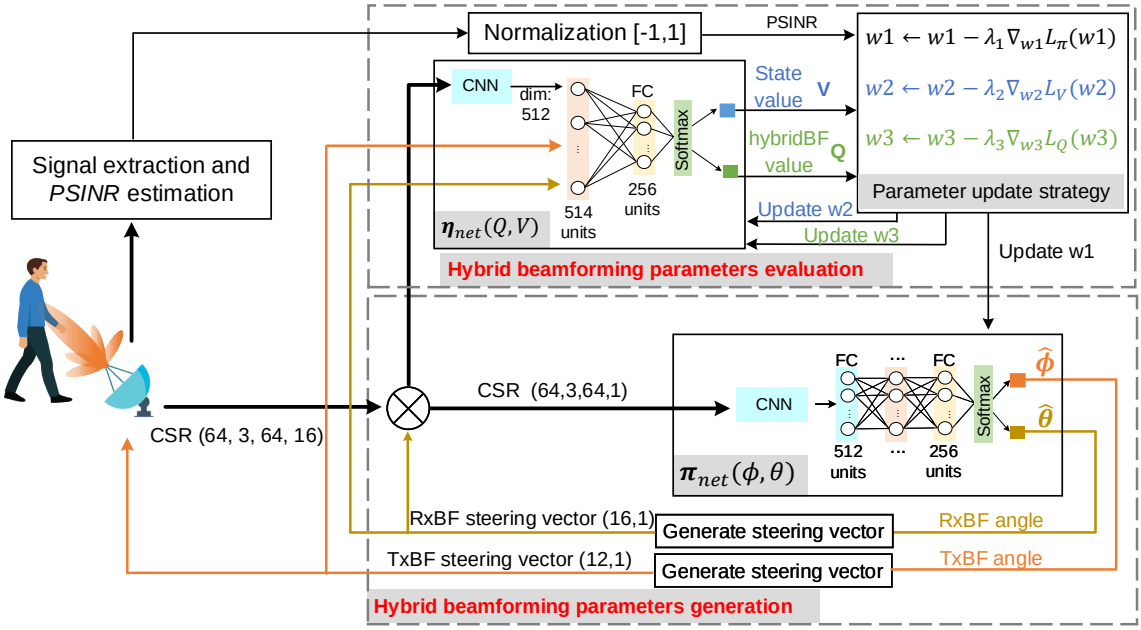

Fig. 14. Beamforming parameters optimization method based on DRL.

generation network, which uses current signal channel state information as observation input, and 2) The hybrid beamforming parameters performance evaluation, which uses beamforming parameters and channel state information to evaluate the value of observation and beamforming parameters.

6.2.1 Hybrid beamforming parameters generation. According to Eq.(12), we want to improve the *PSINR* of the sensed target by searching the transmitter and the receiver beamforming parameters to maximize the received signal channel coefficient. To address this problem, we design a hybrid beamforming parameter generation network $\boldsymbol{\pi}_{net}(\phi)$ to estimate the parameters related to TxBF and RxBF. Unlike established DRL applications, the state signal derived from mmWave radar introduces a heightened level of complexity characterized by high-dimensional received signals. Consequently, traditional network architectures are inadequate for our task directly.

Specifically, we employ the initialized TxBF steering vector (with a steering direction of 0°) to configure the signal transmission direction. Subsequently, the receiver captures the Intermediate Frequency (IF) signal output by the hardware mixer. For the extraction of signal state features, continuous utilization of n frames is employed to construct a four-dimensional vector [Doppler, Frame, Range, Antenna], encapsulating relevant features of the received signals. To derive the Channel State Information (CSI) from the received signal, the Fast Fourier Transform (FFT) is performed separately in the Range and Doppler dimensions, with an FFT size of 64. To address grating lobe interference, as discussed in Section 6.1, the RxBF angle $\hat{\theta}$ is utilized to calculate the beam steering vector for receiver antennas, following Eq. (9). This enhances signal quality in the receiving direction by multiplying the CSI with the RxBF steering vector. The resultant received signal after hybrid beamforming (hybridBF) serves as input for the network $\boldsymbol{\pi}_{net}(\phi)$, responsible for generating parameters associated with hybridBF. Within the network $\boldsymbol{\pi}_{net}(\phi)$, a Convolutional Neural Network (CNN) is employed to encode the 4-dimensional receive signals, resulting in a 512-dimensional feature vector. Subsequently, fully connected layers conduct hybridBF parameter regression, and the softmax function is utilized to obtain the estimation angle of hybridBF, represented as $\hat{\phi}, \hat{\theta}$, as illustrated in Fig.14. Finally, the TxBF angle θ and RxBF angle ϕ are obtained

based on the current CSI from the network $\boldsymbol{\pi}_{net}(\phi, \theta)$. Following this, the next set of received signals is obtained by multiplying the RxBF steering vector with the receive signals without RxBF, according to Eq.(9).

6.2.2 Hybrid beamforming parameters evaluation. To assess the quality of the sensing signal derived from hybridBF parameters $\langle \theta, \phi \rangle$ estimated through the network $\boldsymbol{\pi}_{net}(\omega 1)$, it is worth noting that while employing *PSINR* may offer a straightforward metric to search for an optimal result, it may not necessarily represent the most effective strategy. We expect each search step toward the optimal sensing signal propagation path in every search process. Therefore, we need to design a strategy to guide the parameter generation network $\boldsymbol{\pi}_{net}(\omega 1)$ to search for hybridBF under the optimal sensing path in a faster and more efficient way. To solve this problem, we design an evaluation network $\boldsymbol{\eta}_{net}(Q, V)$ to evaluate the value of hybrid beamforming parameters and the received signals obtained under the current parameters configuration. Specifically, the evaluation network $\boldsymbol{\eta}_{net}(\omega 2, \omega 3)$ receives as input the hybridBF parameters generated by the network $\boldsymbol{\pi}_{net}(\omega 1)$ along with the present channel conditions. It then produces the hybridBF value Q and the status value V as outputs.

To enhance the hybrid beamforming parameter generation network $\boldsymbol{\pi}_{net}(\omega 1)$ so that it more accurately approximates the optimal action decision, we employ the policy extraction technique outlined in SAC [16] for updating the network parameters $\omega 1$, the loss function $L_\pi(\omega 1)$ of policy extraction can be expressed as:

$$L_\pi(\omega 1) = \mathbb{E}_{(s,a)\sim D}[\alpha log(\pi_{\omega 1}(a|s)) - Q_{\omega 3}(s, a)]. \tag{19}$$

Considering that we want the minimum iteration step to obtain the optimal hybrid parameters, we add the step penalty term $\gamma_1 step$ on the hybrid parameter evaluation strategy loss function $L_Q(\omega 3)$. The evaluation network $\boldsymbol{\eta}_{net}(Q, V)$ parameter update method is:

$$\begin{aligned} L_V(\omega 2) &= \mathbb{E}_{(s,a)\sim D}\{L_2[Q_{\omega 3}(s, a) - V(s)]\}, \\ L_Q(\omega 3) &= \mathbb{E}_{(s,a,s')\sim D}[\frac{1}{2}(Q_{\omega 3}(s, a) - (PSINR + \gamma_1 step + \gamma_2 V_{\omega 2}(s')))^2]. \end{aligned} \tag{20}$$

Here, $V(s)$ is a state-value function, $Q_{\omega 3}(s, a)$ is an action-value function, which is the value generated by executing action a based on state s, $L_2[\cdot]$ is L2 norm. $V_{\omega 2}(s')$ is the state-value of the next state s'. γ_2 is a hyperparameters, usually set to 0.99. We train each sample in the dataset until the number of searches reaches 100 steps or the hybridBF parameters corresponding to the maximum *PSINR* are searched. We configure the replay buffer training data pool to include 128 sets of data. During each training iteration, four sets of data are randomly selected, and the parameter optimization strategy is updated every 32 training cycles. The learning rate is set to $3e-4$. This loops through all samples 100 times to fit the best generation network $\boldsymbol{\pi}_{net}(\phi, \theta)$ parameters. Considering that the received signals are 4-dimensional data, we compress the data without losing the data information. We trained our model on four NVIDIA GeForce RTX 3090 for 6 hours, and the results converged significantly. We evaluate the hybrid beamforming parameters generation network using new data that isn't trained.

7 PERFORMANCE EVALUATION

7.1 Experimental Setup

Hardware and software: We evaluate the performance of our framework with a commercial *TI's MMWCAS-RF-EVM* [4] mmWave radar as the sensor and a PC with *Intel(R) Core(TM) i5-7300HQ CPU @2.5GHz* and 16GB RAM as the data processing back end, as shown in Fig.15. The mmWave radar system has 12 transmitter and 16 receiver antennas. It is integrated with a *TI's MMWCAS-DSP-EVM* [3] data capture card to facilitate high-speed data transmission between the mmWave radar and a laptop, and the data transfer speed rate is $5M/s$. We utilize an ER2-ECG monitor[2] to capture the ground truth of ECG measurement. The collected and ground truth data are paired and separated into 30s samples for further processing and evaluation. We write Lua script to connect

and control the mmWave radar and Matlab to preprocess the original mmWave raw data, and write a Python script based on PyTorch to implement the model training and inference. To enhance the reproducibility of the article, we furnish a comprehensive configuration of mmWave wireless signal parameters, elucidated in Table 1.

Table 1. Parameters configuration.

Parameter	Value	Parameter	Value	Parameter	Value
start frequency	$77GHz$	ADC samples	128	number of chips	252
chirp slope	$50MHz/\mu s$	ADC sample frequency	$1000ksps$	range resolution	0.117m
ramp end time	$30us$	idle time	$500\mu s$	Doppler sample frequency	$1680sps$

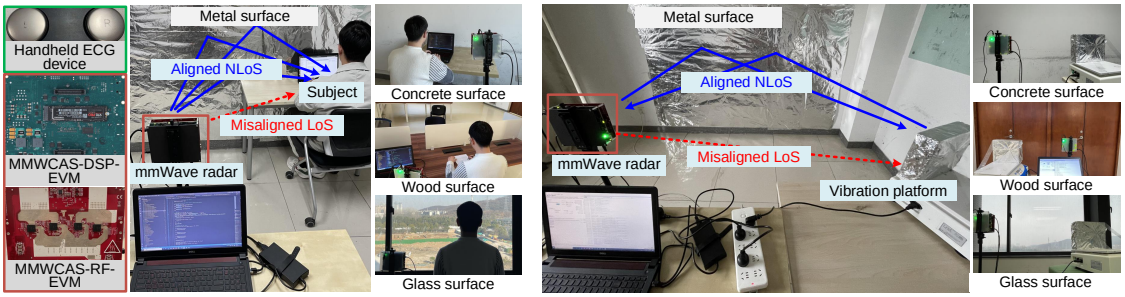

(a) Experimental setup for heartbeat sensing.

(b) Experimental setup for fine-grained motion sensing.

Fig. 15. Experimental setup containing reflective surfaces of various materials (e.g., wood, glass, and concrete).

Datasets: On the other hand, online training is not feasible since the reinforcement learning training cycle is long, and signal acquisition and preprocessing are time-consuming. We make offline datasets to make the network converge quickly. We invite a total of 15 healthy subjects (i.e., 9 males and 6 females) with their ages from 22 to 31. The participants exhibited a range of body mass index (BMI), spanning from 19.6% to 27.4%. During the study, participants were outfitted in regular attire such as sweatshirts, jackets, or T-shirts to ensure their comfort throughout the experimental conditions. Our institution's Institutional Review Board (IRB) has provided ethical approval for this study. Additionally, we ensure that each participant retains the right to be informed about the experiment's content and that their personal data is protected in accordance with privacy regulations. Each participant is required to provide informed consent, acknowledging their understanding of the study's purpose, procedures, risks, and benefits. After reimbursing transportation and other expenses, the financial compensation provided is not less than the hourly wage stipulated by local law. Given that fine-grained motion perception is highly susceptible to interference from large-scale motions (e.g., body motion, walk), to accurately evaluate the performance of the *Trebsen*, volunteers remained stationary in our experimental scene. During data collection, we recommend that volunteers hold the ECG device while either sitting or standing, minimizing large-scale movements to reduce interference by bodily motions. However, during the testing scenario, volunteers are advised to maintain relative stillness and a relaxed posture. The setting emulates a work or study scenario (e.g., as shown in Fig.15(a)), necessitating no additional instructions from the participants. As illustrated in Fig.15, recognizing the variability in the positional alignment among mmWave, reflective surface, and the subject, the resultant reflection paths exhibit distinctions (i.e., the parameters of TxBF and RxBF vary). Therefore, each specific positional relationship is designated as a scene, with experiments involving four common reflective materials: metal, wood, glass, and concrete. We use TxBF to scan the angle $[-60°, +60°]$ in front of the radar as a sample in one scenario. The data dimensions of each sample are (121, 10, 128, 128, 16), representing TxBF angle, frames,

range, doppler, and antenna, respectively. Each sample entails the collection of 1 hour of data, with a resulting data size of 6.7GB. We assemble a dataset comprising 100 sample scenes, encompassing 27 LoS scenarios and 73 NLoS scenarios featuring diverse reflective surfaces (e.g., metal, wood, glass, and concrete). From this dataset, we select 20 scenes to constitute an evaluation set. In order to verify the generalization of *Trebsen*, we additionally collect 20 NLoS scenes under four types of reflective materials as a test set to evaluate the performance of the *Trebsen*.

Scheme metrics: To evaluate the performance of the scheme's search for optimal beamforming parameters, we use the search latency and *PISNR* of the fine-grained motion signal. For example, the vibration frequency error estimate of the vibration platform can be expressed as: $Vib_{err} = \frac{|Vib_{gt} - Vib_{est}|}{Vib_{gt}} \times 100\%$.

Application metrics: We use Heart Rate(HR) Estimation Error [35] and Inter-Beat Interval(IBI) Estimation Error as evaluation metrics in heartbeat detection applications. For example, the heart rate estimation error calculation formula can be expressed as: $HR_{err} = \frac{abs(HR_{gt} - HR_{est})}{HR_{gt}} * 100\%$.

7.2 Overall Performance

To evaluate the performance of the *Trebsen*, a Transmitter-REceiver collaboration-based Beamforming scheme SENsing using commercial mmWave radars, we design experiments to compare the performance of the traditional method, which is single transmitting and single receiving without beamforming, and *Trebsen* in the LoS misaligned scenario.

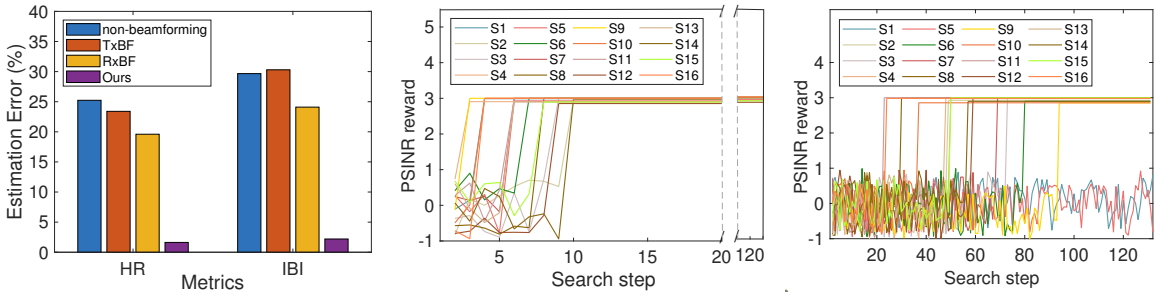

(a) Heartbeat estimation error. (b) *Trebsen* search method. (c) Random search method.

Fig. 16. Overall performance for *Trebsen*: (a) comparison of heartbeat estimation error between *Trebsen* and other beamforming methods, (b) DRL-based search speed in the *Trebsen* scheme, (c) Random search speed in the *Trebsen* scheme.

The performance of heartbeat monitoring based on *Trebsen*. We evaluate the performance of *Trebsen* at the scheme level and in a typical fine-grained sensing application (i.e., heartbeat monitoring). In applications, we design heartbeat sensing experiments, fix the distance and orientation between the mmWave radar and the user. Specifically, The wall covered with tin foil serves as a simulation of a metal reflective surface. The positional relationship between the mmWave radar and the volunteers is depicted in Fig.15(a). By establishing an NLoS path, the perceived signal quality is enhanced, particularly when the LoS path is blocked or misaligned. We use the *Trebsen*, TxBF only, RxBF only, and non-beamforming to obtain the heartbeat signal in the scene where the LoS is obstructed or misaligned, as shown in Fig.15(a). As shown in Fig.16(a), the average heart rate (HR) error of *Trebsen* is 1.63%, and the average inter-beat interval (IBI) error is 2.20%, the average HR and IBI errors of *Trebsen* are reduced by 23.6% and 27.47% compared with traditional methods, respectively. The experimental results show that the *Trebsen* ingeniously constructed an NLoS propagation path through the utilization of such reflections in scenarios where LoS propagation was obstructed or misaligned. To ensure the validity of the experiments, no special requirements are imposed regarding participants' clothing, gender, age, BMI, etc. The experimental

results indicate that variations in participants' clothing, gender, and age do not affect the experimental outcomes. While participants with different BMIs do show slight variations in experimental results, these differences are not statistically significant. The *Trebsen*, by constructing an NLoS path, significantly improves the perceived signal quality in scenarios where LoS is blocked or misaligned. *Experimental results show that the* Trebsen *substantially enhances fine-grained motion-sensing performance by constructing a primary NLoS propagation path, particularly in scenarios where LoS is blocked or misaligned.*

The performance of search method based on *Trebsen*. To further evaluate the performance of *Trebsen*, we design comparative experiments to evaluate the performance of the random-based search method and the *Trebsen*. Specifically, as shown in Fig.15(b), we design fine-grained motion sensing experiments, fix the distance and orientation between the mmWave radar and the platform, the wall covered with tin foil simulates a metal reflective surface. We utilize a vibration platform to simulate fine-grained movement, setting its vibration frequency to 75 cycles per minute. By establishing a NLoS path, the perceived signal quality is enhanced, particularly when the LoS path is misaligned (i.e., the direction of the radar and the target motion may be misaligned). We scan the range of angle space $[-60°, 60°]$ using TxBF, and the RxBF angle is consistent with the TxBF angle in each scan, one scan result is used as a sample to evaluate the performance of the search algorithm. We collect 20 samples as a test set and use random search and *Trebsen* to search for the optimal *PSINR* value, moreover, to facilitate comparison, we normalize the *PSINR* values. As shown in Fig.16(b) and Fig.16(c), Experiment results show that the *Trebsen* can find the optimal *PSINR* value less ten steps, but the random search method takes more than 40 steps on average, and its variance is large, making it difficult to guarantee the stability of the search results. Compared with random search, the *Trebsen* exhibits a 90% increase in search speed. *Experimental results show that* Trebsen *while significantly enhancing the performance of fine-grained motion sensing, its search speed is* 90% *faster than the random algorithm*

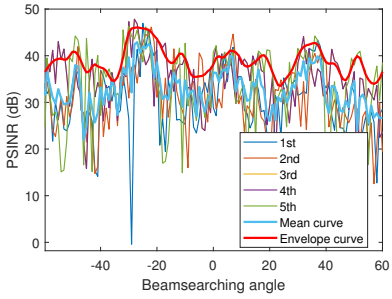

Fig. 17. Effectiveness and robustness of *PSINR* metric.

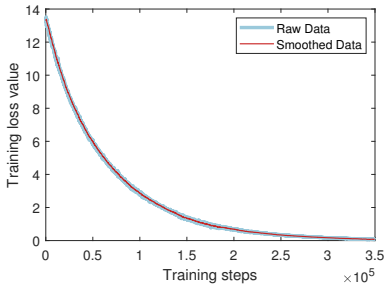

Fig. 18. Effectiveness of parameters search method based on DRL.

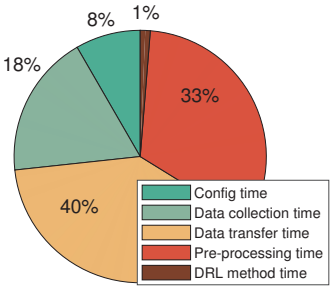

Fig. 19. The time consumption proportion of sub-module in *Trebsen*.

7.3 Effectiveness and Robustness Study

We evaluate the effectiveness and robustness of *PSINR* metric and hybridBF parameter search method for a hybrid beamforming scheme.

7.3.1 Effectiveness and robustness of PSINR *metric.* To evaluate the effectiveness and robustness of the *PSINR* metric, we tested it five times in one scenario. Specifically, as shown in the single-target motion experiment scenario in Fig. 15(b), we scan the range of angle space $[-60°, 60°]$ using TxBF, and the RxBF angle is consistent with the TxBF angle in each scan. As shown in Fig.17, through multiple tests, we observed that the target position remains consistently stable, with its highest peak exhibiting a minimum $3dB$ difference from the *PSINR* values of other peaks. Additionally, the mean TxBF angle across various experiments is $-25°$, with a variance of $5°$. The

experimental outcomes demonstrate that our proposed *PSINR* metric presents notable advantages in applications focused on measuring fine-grained target sensing.

7.3.2 Effectiveness of hybridBF parameters search method based on DRL. To assess the efficacy and robustness of the hybridBF parameters search method in *Trebsen*, as illustrated in Fig. 18, we monitored the policy loss curve throughout the training process. We conducted training for each sample in the dataset until the number of searches reached 100 steps or the hybridBF parameters corresponding to the maximum *PSINR* were identified. For the configuration of the replay buffer training data pool, we included 128 sets of data. During each training iteration, four sets of data were randomly selected, and the parameter optimization strategy was updated every 32 training cycles. *Experimental results show that the loss value of* Trebsen *quickly converges to zero and remains stable during the training and remains stable in the subsequent process.*

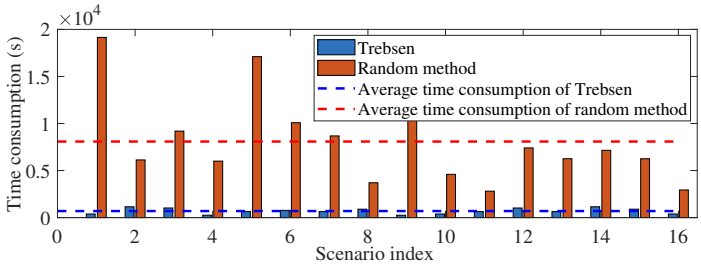

Fig. 20. Comparison of time consumption using *Trebsen* and random search method in 16 scenarios.

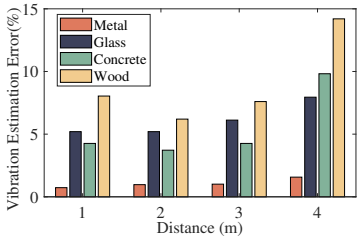

Fig. 21. Comparison of fine-grained motion estimation errors across various reflective materials.

7.3.3 Analysis of time efficiency. To comprehensively assess the time consumption of *Trebsen*, we conduct experiments to measure the time consumption of each sub-module and compare it with a random search. The experimental setup is shown in Fig.15(a). We invite five volunteers to collect 30*s* respiratory and heartbeat data in each of the 16 scenarios. As shown in Fig.19, the average time consumption for one iteration of the *Trebsen* is about 179.73 seconds. This breakdown includes 15 seconds for hardware configuration, 33 seconds for data collection, 71.48 seconds for data transfer at a rate of $5M/s$, and the data preprocessing stage consumes 58.43 seconds. The overall time consumption is distributed among various processes, with the following proportions: 8% for hardware configuration, 18% for data collection, 40% for data transfer, and 33% for data preprocessing. The DRL-based search methods contribute only 1% (i.e., 2.3s) to the total time consumption, indicating that *Trebsen* does not significantly incur excessive time consumption. As shown in Fig.20, we find that the *Trebsen* significantly improved time consumption compared to a random search for the optimal sensing path in 16 scenarios. Experimental results show that the random method requires approximately 8081 seconds to find the optimal sensing path, whereas *Trebsen* accomplishes the task in about 694 seconds, resulting in a 91.4% reduction in time consumption.

7.3.4 The impact of different reflective materials on Trebsen *performance.* To comprehensively investigate the influence of diverse reflective materials on *Trebsen*'s performance in NLoS scenes, we conducted comparative experiments in different reflective surface scenes. These experiments aimed to explore the impact of various materials on fine-grained target perception performance in NLoS scenarios. The experimental setup, depicted in Fig.15(b), involved selecting four common materials—metal, glass windows, concrete walls, and wooden doors. We chose these common materials to assess their impact on *Trebsen*'s performance in the experimental scene. The distance between the vibration platform and the reflected surface varied from 0.5m to 2m, while the distance between the radar and the reflected surface also varied from 0.5m to 2m. We collected data over a 10-second

period to estimate the speed of the vibration platform (with a ground truth of 78 times per minute). As illustrated in Fig.21, the experimental findings demonstrate that metal materials exhibit lower estimation errors compared to other materials, boasting an average estimation error of 1.09%. In contrast, glass windows and wooden doors exhibit higher estimation errors due to severe transmission losses.

7.4 Case Study: Heartbeat Sensing

To verify the practicality of *Trebsen* in applications, we evaluate the performance with a typical heartbeat detection application. We devised experiments to evaluate the sensing performance of both the non-beamforming and the *Trebsen* across varying distances and relative position relationships between mmWave radar and the user.

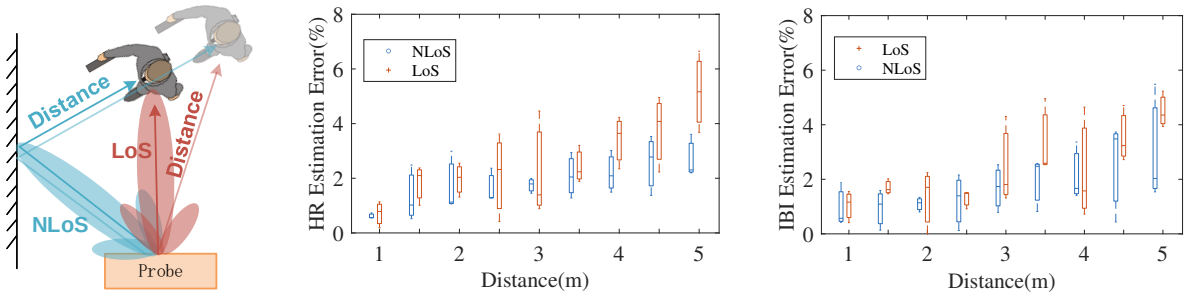

(a) Location relationships. (b) Impact of distance on HR error. (c) Impact of distance on IBI error.

Fig. 22. The impact of signal propagation distance on the performance of *Trebsen* in NLoS and LoS scenarios.

7.4.1 Impact of Sensing Distance. Sensing distance is a key factor affecting the robustness of fine-grained target sensing based on mmWave radar. Therefore, we undertake a series of experiments to evaluate the performance of *Trebsen* across varying sensing distances within both LoS and NLoS scenarios. Specifically, we invited five volunteers to participate in experiments, and the distance between the volunteer and mmWave radar is set from $1m$ to $5m$ with a $0.5m$ distance step, as shown in Fig.22(a). The results in Fig.22(b) and Fig.22(c) show that the error of *Trebsen* increases with the increase of distance, but the perceptual performance of NLoS path is always lower than that of LoS path. *The experimental results indicate that when the LoS is weakened, the heartbeat perception error substantially increases with the non-beamforming method. In contrast, the* Trebsen *demonstrates the ability to maintain a consistently low error under similar conditions.*

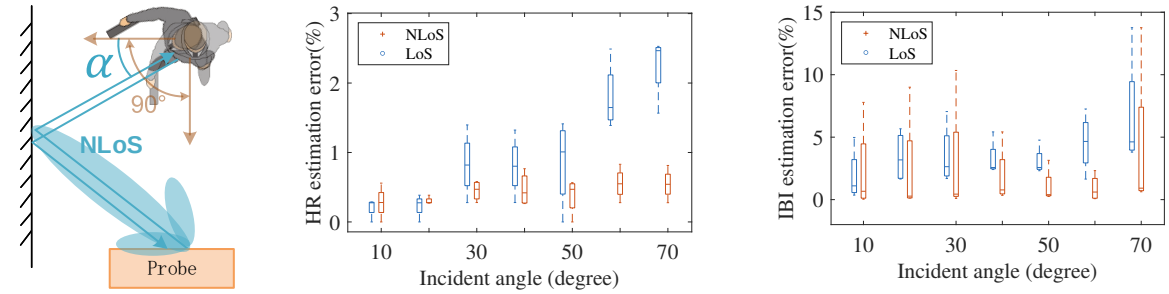

(a) Location relationships. (b) Impact of incident angle on HR error. (c) Impact of incident angle on IBI error.

Fig. 23. The impact of incident angle on the performance of *Trebsen* in NLoS and LoS scenarios.

7.4.2 Impact of Incident Angle. In order to explore the impact of incident angle on *Trebsen*'s perceptual performance, we designed experiments to compare the perceptual performance of LoS and NLoS in the same scene. Specifically, we invited five volunteers to participate in the experiment, the signal perception distance between the volunteers and the probe was set to 2m, and the incident angle between the volunteers and the probe was from 10° to 70° changes, as shown in the figure 23(a). The results in Fig.23(b) show that when the incident angle varies from 10° to 70°, the HR estimation error based is less than 1% in the NLoS perception path, while the HR estimation error is increase significantly in the LoS path. As shown in Fig.23(c), we observed that the IBI estimation error in the LoS path increases significantly with increasing incident angle, while the average perceived IBI estimation error in the NLoS path remains stable and less than 5%. The reason is that when the incident angle increases in the NLoS scene, the sensing accuracy can be improved by fine-tuning the beamforming signal transmitting angle to change the incident angle. However, in LoS scenarios, the signal attenuation caused by the incident angle increases significantly as the incident angle increases, resulting in reduced sensing accuracy. *Experimental results show that as the incident angle increases from* 10° *to* 70°, Trebsen *can show extremely low average HR or IBI estimation errors in both LoS and NLoS scenarios.*

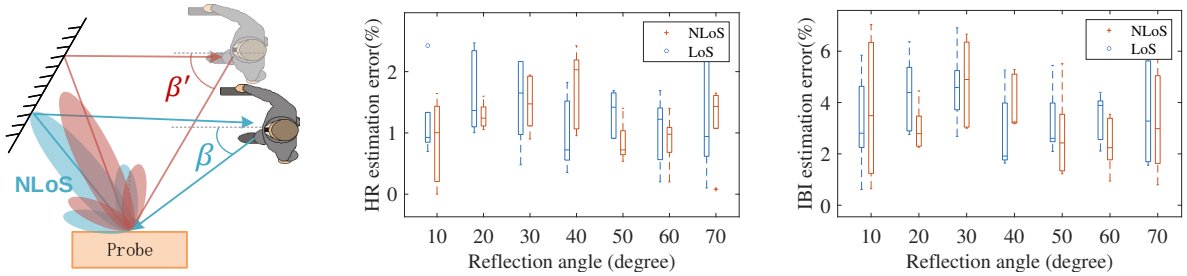

(a) Location relationships. (b) Impact of reflection angle on HR error. (c) Impact of reflection angle on IBI error.

Fig. 24. The impact of reflection angle on the performance of *Trebsen* in NLoS and LoS scenarios.

7.4.3 Impact of Reflection Angle. In order to explore the impact of reflection angle on *Trebsen*'s perceptual performance, we designed experiments to compare the perceptual performance of LoS and NLoS in the same scene. Specifically, we invited five volunteers to participate in the experiment, the reflection angle between the volunteers and the probe was from 10° to 70° changes, and the signal perception distance between the volunteer and the probe is set to 2*m* each time, as shown in the figure 24(a). The outcomes presented in Figure 24(b) indicate that as the reflection angle ranges from 10° to 70°, the average estimation error for Heart Rate (HR) remains consistently at 1% for both LoS and NLoS scenarios. *Experimental results show that as the reflection angle increases from* 10° *to* 70°, Trebsen *can show extremely low average HR or IBI estimation errors in both LoS and NLoS scenarios.*

7.4.4 The impact of different reflective materials on Trebsen *performance.* To assess the influence of reflective materials on sensing performance in NLoS scenarios, particularly for heartbeat perception, we conducted a comparative experiment. We invited five volunteers (two males and three females) to participate in the experiment, exploring heartbeat perception under various reflective materials. We select four common materials in daily life, including metal, glass, concrete, and wood, as reflective surfaces. We invite volunteers to face the mmWave radar 1.5m away from the wall. Their positional relationship is shown in Fig.15(a). We collect heartbeat data from volunteers for 10 seconds to estimate their HR and IBI. The experimental results, as depicted in Fig. 25, highlight the significant impact of different reflective materials on *Trebsen*'s performance. Notably, its advantages are more pronounced when dealing with metal-reflective materials. However, the severe transmission signal attenuation observed with wooden materials leads to a notable increase in estimation error.

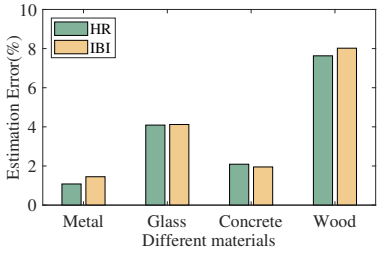

Fig. 25. Comparison of HR/IBI estimation errors in different NLoS reflective material scenarios.

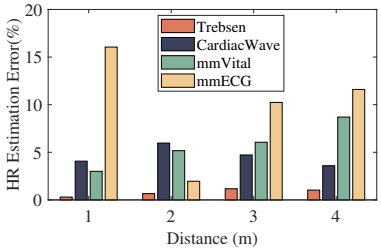

Fig. 26. Comparison of HR estimation errors between *Trebsen* and SoTA methods.

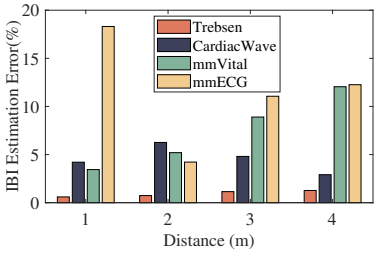

Fig. 27. Comparison of IBI estimation errors between *Trebsen* and SoTA methods.

7.4.5 Comparing performance between Trebsen *and SoTA methods.* To highlight the performance advantages of *Trebsen* in fine-grained sensing applications (e.g., respiration and heartbeat), we conducted comparative experiments against existing State-of-the-Art (SoTA) methods, including mmVital [18], CardiacWave [33], and mmECG [35]. Specifically, in the experimental setting, depicted in Fig.15(a), volunteers and the radar are positioned side by side facing a wall. The distance between volunteers and the wall varies from 0.5m to 2m, while the distance between the radar and the wall also varies from 0.5m to 2m. Therefore, the propagation distance of the NLoS signal through the reflected surface varies from 1m to 4m. Besides, to control experimental variables and guarantee the validity of the results, we employ the same hardware (i.e., *TI MMWCAS-RF-EVM*) and radar signal parameter configuration, as illustrated in Table 1. In Fig.26 and Fig.27, we compare the HR and IBI estimation errors of different methods as the distance increases. The experimental results reveal that our scheme achieves an average HR estimation error of about 1%, demonstrating a 9.17% reduction over mmECG [35] and a 3.8% reduction over CardiacWave [33]. These findings underscore the superiority of *Trebsen* compared to SoTA methods, with substantial reductions in both HR and IBI estimation errors. This improvement can be attributed to the fact that *Trebsen* leverages surrounding reflective surfaces to construct an NLoS signal propagation path, thereby enhancing perceived signal quality, particularly in scenarios where the LoS path weakens. *The experimental results demonstrate that as the distance increases,* Trebsen*'s HR and IBI estimation errors consistently outperform those of the SoTA method.*

8 LIMITATION & DISCUSSION

Limitations. Although the NLoS propagation path established through *Trebsen* enhances perceptual performance in scenarios where the LoS path is obstructed or misaligned, there are still some limitations when implementing this approach in real environments. (1) Due to the limitation on the sensing distance of mmWave radar, the users are supposed to be close to the radar (within 5m) for accurate and efficient fine-grained motion sensing. Based on the understanding, indoor fine-grained motion sensing is more suitable, where the mmWave antenna can cover the primary activity area in the room. Therefore, to obtain a larger sensing range, increase the number of antennas to obtain a longer beamforming signal propagation distance. (2) Since the essential principle of *Trebsen* is to use the multipath effect of wireless signals, when the LoS scene is occluded or weakened, an NLoS path is constructed by using the environmental specular reflection to obtain fine-grained motion sensing. Therefore, the reflection coefficient $\mathbf{h}_{sf}$ of the multipath reflection surface in the environment will also affect the sensing performance. This shortcoming limits the application scenarios of the *Trebsen*. (3) Considering that the time consumption of a single fine-grained sensing operation is associated with the specific target (e.g., 30s heartbeat sensing generates approximately 800 MByte of data), coupled with the current limitation of the data transmission rate to 5 M/s and the time consumption of data preprocessing, the delay in a single search operation

is relatively significant. Therefore, reducing data transmission and preprocessing delays is crucial to improving the generalization performance of *Trebsen*, and this will be further optimized in the future.

Discussion. Currently, we propose *Trebsen*, a Transmitter-REceiver collaboration-based Beamforming scheme SENsing using commercial mmWave radars. In this section, we aim to delve into the potential practical applications of our proposed method, *Trebsen*, a Transmitter-REceiver collaboration-based Beamforming scheme SENsing utilizing commercial mmWave radars. One key strength of *Trebsen* lies in its ability to construct an NLoS signal propagation path, enabling optimal fine-grained motion sensing in scenarios where LoS is occluded or weakened. This characteristic makes *Trebsen* particularly well-suited for diverse real-world applications. To enhance the robustness and generalizability of *Trebsen*, we are actively exploring its application in various fine-grained motion-sensing scenarios. Specifically: (1) We use *Trebsen* in other fine-grained motion sensing applications, e.g., gesture recognition and handwriting tracking, to further improve the robustness and generalization of the *Trebsen*. (2) Additionally, we are exploring the integration of *Trebsen* in voice recognition applications. The precise beamforming and optimal signal propagation paths provided by *Trebsen* could contribute to enhanced voice recognition accuracy, especially in scenarios where LoS communication is obstructed or misaligned. (3) Another promising avenue for *Trebsen* is in the realm of automotive in-cabin monitoring. The precise beamforming and optimal signal propagation paths provided by *Trebsen* could be instrumental in achieving fine-grained perception for monitoring passengers in a vehicle's cabin. This application holds significant importance for enhancing safety and comfort in automotive environments, especially in scenarios where traditional monitoring methods may face challenges.

In the future, our focus extends to further optimizing the hybrid beamformer parameters within *Trebsen*. This optimization not only aims to achieve lower latency but also seeks to enhance the effectiveness of gradient strategies. These improvements are envisioned to bolster the performance of *Trebsen* in real-world scenarios, making it a versatile and reliable solution for diverse applications.

9 CONCLUSION

Previous solutions based on mmWave sensing have often assumed a reliable signal quality. Nevertheless, ensuring an unobstructed LoS path is challenging, making it crucial to identify NLoS paths to enhance perceived signal quality. Therefore, we propose *Trebsen*, a Transmitter-REceiver collaboration-based Beamforming scheme SENsing using commercial mmWave radars. First, we define the hybrid beamforming problem as an optimization challenge involving beamforming angle search based on transmitter-receiver collaboration, and we derive a comprehensive expression for parameter optimization by modeling the signal attenuation variations resulting from the incident and reflection angles. Second, we design a novel metric *PSINR*, combining the carrier signal and baseband signal to quantify the fine-grained sensing motion signal quality. Third, We employ a parameter search method based on deep reinforcement learning (DRL) to search optimal beamforming angles at both transmitter and receiver quickly. We have implemented *Trebsen* and evaluated its performance. In specific applications, experimental results show that *Trebsen* significantly enhances heartbeat sensing performance in scenes with occluded or weakened LoS. Compared to non-beamforming, *Trebsen* demonstrates a reduction of 23.6% in average HR error and 27.47% in average IBI error. Moreover, we verified the search performance of *Trebsen*, compared with random search, *Trebsen* exhibits a 90% increase in search speed.

ACKNOWLEDGMENT

This work is supported in part by National Key Research and Development Program of China under Grant No.2022YFB3303900; National Natural Science Foundation of China under Grant No. 62272216, 62372224; Collaborative Innovation Center of Novel Software Technology and Industrialization. Lei Xie is the corresponding author.

REFERENCES

[1] 2023. AWR6843 single-chip 60-GHz to 64-GHz automotive radar sensor. [Online]. https://www.ti.com/tool/AWR6843ISK.

[2] 2023. Handheld and Wearable ECG Monitor ER2. [Online]. https://www.viatomtech.com/er2.

[3] 2023. mmWave cascade imaging radar DSP evaluation module. [Online]. https://www.ti.com/tool/MMWCAS-DSP-EVM.

[4] 2023. mmWave cascade imaging radar RF evaluation module. [Online]. https://www.ti.com/tool/MMWCAS-DSP-EVM.

[5] Mohammed Abdelghany, Ali A. Farid, Maryam Eslami Rasekh, Upamanyu Madhow, and Mark J. W. Rodwell. 2021. A Design Framework for All-Digital mmWave Massive MIMO With per-Antenna Nonlinearities. *IEEE Transactions on Wireless Communications* 20, 9 (2021), 5689–5701. https://doi.org/10.1109/TWC.2021.3069378

[6] Aakriti Adhikari, Hem Regmi, Sanjib Sur, and Srihari Nelakuditi. 2022. MiShape: Accurate Human Silhouettes and Body Joints from Commodity Millimeter-Wave Devices. *Proc. ACM Interact. Mob. Wearable Ubiquitous Technol.* 6, 3, Article 96 (sep 2022), 31 pages. https://doi.org/10.1145/3550300

[7] D. Berry, R. Malech, and W. Kennedy. 1963. The reflectarray antenna. *IEEE Transactions on Antennas and Propagation* 11, 6 (1963), 645–651. https://doi.org/10.1109/TAP.1963.1138112

[8] Dongjiang Cao, Ruofeng Liu, Hao Li, Shuai Wang, Wenchao Jiang, and Chris Xiaoxuan Lu. 2022. Cross Vision-RF Gait Re-Identification with Low-Cost RGB-D Cameras and MmWave Radars. *Proc. ACM Interact. Mob. Wearable Ubiquitous Technol.* 6, 3, Article 102 (sep 2022), 25 pages. https://doi.org/10.1145/3550325

[9] Baicheng Chen, Huining Li, Zhengxiong Li, Xingyu Chen, Chenhan Xu, and Wenyao Xu. 2020. ThermoWave: A New Paradigm of Wireless Passive Temperature Monitoring via MmWave Sensing. In *Proceedings of the 26th Annual International Conference on Mobile Computing and Networking* (London, United Kingdom) *(MobiCom '20)*. Association for Computing Machinery, New York, NY, USA, Article 27, 14 pages. https://doi.org/10.1145/3372224.3419184

[10] V.C. Chen, F. Li, S.-S. Ho, and H. Wechsler. 2006. Micro-Doppler effect in radar: phenomenon, model, and simulation study. *IEEE Trans. Aerospace Electron. Systems* 42, 1 (2006), 2–21. https://doi.org/10.1109/TAES.2006.1603402

[11] Peter Delos, Bob Broughton, and Jon Kraft. 2020. Phased array antenna patterns—part 2: grating lobes and beam squint. *Analog Dialogue* 54, 2 (2020), 1–4.

[12] Long Fan, Lei Xie, Xinran Lu, Yi Li, Chuyu Wang, and Sanglu Lu. 2023. mmMIC: Multi-modal Speech Recognition based on mmWave Radar. In *IEEE INFOCOM 2023 - IEEE Conference on Computer Communications*. IEEE INFOCOM 2023, New York City, NY, USA, 1–10. https://doi.org/10.1109/INFOCOM53939.2023.10229085

[13] Yiwen Feng, Kai Zhang, Chuyu Wang, Lei Xie, Jingyi Ning, and Shijia Chen. 2023. mmEavesdropper: Signal Augmentation-based Directional Eavesdropping with mmWave Radar. In *IEEE INFOCOM 2023 - IEEE Conference on Computer Communications*. IEEE INFOCOM 2023, New York City, NY, USA, 1–10. https://doi.org/10.1109/INFOCOM53939.2023.10229095

[14] H.T. Friis. 1946. A Note on a Simple Transmission Formula. *Proceedings of the IRE* 34, 5 (1946), 254–256. https://doi.org/10.1109/JRPROC.1946.234568

[15] A.B. Gershman, E. Nemeth, and J.F. Bohme. 2000. Experimental performance of adaptive beamforming in a sonar environment with a towed array and moving interfering sources. *IEEE Transactions on Signal Processing* 48, 1 (2000), 246–250. https://doi.org/10.1109/78.815495

[16] Tuomas Haarnoja, Aurick Zhou, Pieter Abbeel, and Sergey Levine. 2018. Soft Actor-Critic: Off-Policy Maximum Entropy Deep Reinforcement Learning with a Stochastic Actor. *CoRR* abs/1801.01290 (2018). arXiv:1801.01290 http://arxiv.org/abs/1801.01290

[17] Shuangfeng Han, Chih-lin I, Zhikun Xu, and Corbett Rowell. 2015. Large-scale antenna systems with hybrid analog and digital beamforming for millimeter wave 5G. *IEEE Communications Magazine* 53, 1 (2015), 186–194. https://doi.org/10.1109/MCOM.2015.7010533

[18] Srikrishna Iyer, Leo Zhao, Manoj Prabhakar Mohan, Joe Jimeno, Mohammed Yakoob Siyal, Arokiaswami Alphones, and Muhammad Faeyz Karim. 2022. mm-Wave Radar-Based Vital Signs Monitoring and Arrhythmia Detection Using Machine Learning. *Sensors* 22, 9 (2022). https://doi.org/10.3390/s22093106

[19] Matthias Kronauge and Hermann Rohling. 2013. Fast Two-Dimensional CFAR Procedure. *IEEE Trans. Aerospace Electron. Systems* 49, 3 (2013), 1817–1823. https://doi.org/10.1109/TAES.2013.6558022

[20] Jaime Lien, Nicholas Gillian, M. Emre Karagozler, Patrick Amihood, Carsten Schwesig, Erik Olson, Hakim Raja, and Ivan Poupyrev. 2016. Soli: Ubiquitous Gesture Sensing with Millimeter Wave Radar. *ACM Trans. Graph.* 35, 4, Article 142 (jul 2016), 19 pages. https://doi.org/10.1145/2897824.2925953

[21] Haipeng Liu, Yuheng Wang, Anfu Zhou, Hanyue He, Wei Wang, Kunpeng Wang, Peilin Pan, Yixuan Lu, Liang Liu, and Huadong Ma. 2020. Real-Time Arm Gesture Recognition in Smart Home Scenarios via Millimeter Wave Sensing. *Proc. ACM Interact. Mob. Wearable Ubiquitous Technol.* 4, 4, Article 140 (dec 2020), 28 pages. https://doi.org/10.1145/3432235

[22] Jia Liu, Min Chen, Shigang Chen, Qingfeng Pan, and Lijun Chen. 2017. Tag-compass: Determining the spatial direction of an object with small dimensions. In *IEEE INFOCOM 2017 - IEEE Conference on Computer Communications*. 1–9. https://doi.org/10.1109/INFOCOM.2017.8057159

[23] Tiantian Liu, Ming Gao, Feng Lin, Chao Wang, Zhongjie Ba, Jinsong Han, Wenyao Xu, and Kui Ren. 2021. Wavoice: A Noise-Resistant Multi-Modal Speech Recognition System Fusing MmWave and Audio Signals. In *Proceedings of the 19th ACM Conference on Embedded*

Networked Sensor Systems (Coimbra, Portugal) *(SenSys '21)*. Association for Computing Machinery, New York, NY, USA, 97–110. https://doi.org/10.1145/3485730.3485945

[24] Chris Xiaoxuan Lu, Muhamad Risqi U. Saputra, Peijun Zhao, Yasin Almalioglu, Pedro P. B. de Gusmao, Changhao Chen, Ke Sun, Niki Trigoni, and Andrew Markham. 2020. MilliEgo: Single-Chip MmWave Radar Aided Egomotion Estimation via Deep Sensor Fusion. In *Proceedings of the 18th Conference on Embedded Networked Sensor Systems* (Virtual Event, Japan) *(SenSys '20)*. Association for Computing Machinery, New York, NY, USA, 109–122. https://doi.org/10.1145/3384419.3430776

[25] Andreas F. Molisch, Vishnu V. Ratnam, Shengqian Han, Zheda Li, Sinh Le Hong Nguyen, Linsheng Li, and Katsuyuki Haneda. 2017. Hybrid Beamforming for Massive MIMO: A Survey. *IEEE Communications Magazine* 55, 9 (2017), 134–141. https://doi.org/10.1109/MCOM.2017.1600400

[26] Panneer Selvam Santhalingam, Al Amin Hosain, Ding Zhang, Parth Pathak, Huzefa Rangwala, and Raja Kushalnagar. 2020. MmASL: Environment-Independent ASL Gesture Recognition Using 60 GHz Millimeter-Wave Signals. *Proc. ACM Interact. Mob. Wearable Ubiquitous Technol.* 4, 1, Article 26 (mar 2020), 30 pages. https://doi.org/10.1145/3381010

[27] Zhenguo Shi, Tao Gu, Yu Zhang, and Xi Zhang. 2023. MmBP: Contact-Free Millimetre-Wave Radar Based Approach to Blood Pressure Measurement. In *Proceedings of the 20th ACM Conference on Embedded Networked Sensor Systems* (Boston, Massachusetts) *(SenSys '22)*. Association for Computing Machinery, New York, NY, USA, 667–681. https://doi.org/10.1145/3560905.3568506

[28] Mohsen Tajallifar, Ahmad R. Sharafat, and Halim Yanikomeroglu. 2023. Robust and Feasible QoS-Aware mmWave Massive MIMO Hybrid Beamforming. *IEEE Transactions on Wireless Communications* (2023), 1–1. https://doi.org/10.1109/TWC.2023.3290141

[29] Chao Wang, Feng Lin, Zhongjie Ba, Fan Zhang, Wenyao Xu, and Kui Ren. 2022. Wavesdropper: Through-Wall Word Detection of Human Speech via Commercial MmWave Devices. *Proc. ACM Interact. Mob. Wearable Ubiquitous Technol.* 6, 2, Article 77 (jul 2022), 26 pages. https://doi.org/10.1145/3534592

[30] Chuyu Wang, Lei Xie, Keyan Zhang, Wei Wang, Yanling Bu, and Sanglu Lu. 2019. Spin-Antenna: 3D Motion Tracking for Tag Array Labeled Objects via Spinning Antenna. In *IEEE INFOCOM 2019 - IEEE Conference on Computer Communications*. 1–9. https://doi.org/10.1109/INFOCOM.2019.8737372

[31] Teng Wei and Xinyu Zhang. 2015. MTrack: High-Precision Passive Tracking Using Millimeter Wave Radios. In *Proceedings of the 21st Annual International Conference on Mobile Computing and Networking* (Paris, France) *(MobiCom '15)*. Association for Computing Machinery, New York, NY, USA, 117–129. https://doi.org/10.1145/2789168.2790113

[32] Chenshu Wu, Feng Zhang, Beibei Wang, and K. J. Ray Liu. 2020. MmTrack: Passive Multi-Person Localization Using Commodity Millimeter Wave Radio. In *IEEE INFOCOM 2020 - IEEE Conference on Computer Communications* (Toronto, ON, Canada). IEEE Press, 2400–2409. https://doi.org/10.1109/INFOCOM41043.2020.9155293

[33] Chenhan Xu, Huining Li, Zhengxiong Li, Hanbin Zhang, Aditya Singh Rathore, Xingyu Chen, Kun Wang, Ming-chun Huang, and Wenyao Xu. 2021. CardiacWave: A MmWave-Based Scheme of Non-Contact and High-Definition Heart Activity Computing. *Proc. ACM Interact. Mob. Wearable Ubiquitous Technol.* 5, 3, Article 135 (sep 2021), 26 pages. https://doi.org/10.1145/3478127

[34] Weiye Xu, Wenfan Song, Jianwei Liu, Yajie Liu, Xin Cui, Yuanqing Zheng, Jinsong Han, Xinhuai Wang, and Kui Ren. 2022. Mask Does Not Matter: Anti-Spoofing Face Authentication Using MmWave without on-Site Registration. In *Proceedings of the 28th Annual International Conference on Mobile Computing And Networking* (Sydney, NSW, Australia) *(MobiCom '22)*. Association for Computing Machinery, New York, NY, USA, 310–323. https://doi.org/10.1145/3495243.3560515

[35] Xiangyu Xu, Jiadi Yu, Chengguang Ma, Yanzhi Ren, Hongbo Liu, Yanmin Zhu, Yi-Chao Chen, and Feilong Tang. 2022. MmECG: Monitoring Human Cardiac Cycle in Driving Environments Leveraging Millimeter Wave. In *IEEE INFOCOM 2022 - IEEE Conference on Computer Communications* (London, United Kingdom). IEEE Press, 90–99. https://doi.org/10.1109/INFOCOM48880.2022.9796912

[36] Hongfei Xue, Qiming Cao, Yan Ju, Haochen Hu, Haoyu Wang, Aidong Zhang, and Lu Su. 2023. M4esh: MmWave-Based 3D Human Mesh Construction for Multiple Subjects. In *Proceedings of the 20th ACM Conference on Embedded Networked Sensor Systems* (Boston, Massachusetts) *(SenSys '22)*. Association for Computing Machinery, New York, NY, USA, 391–406. https://doi.org/10.1145/3560905.3568545

[37] Cunzhuo Zhao, Yunlong Cai, An Liu, Minjian Zhao, and Lajos Hanzo. 2020. Mobile Edge Computing Meets mmWave Communications: Joint Beamforming and Resource Allocation for System Delay Minimization. *IEEE Transactions on Wireless Communications* 19, 4 (2020), 2382–2396. https://doi.org/10.1109/TWC.2020.2964543

[38] Xin Zhao, Xue Jia, Tao Zhang, Yahui Cao, and Tianwei Liu. 2023. Evolutionary Algorithms With Blind Fitness Evaluation for Solving Optimization Problems With Only Fuzzy Fitness Information. *IEEE Transactions on Fuzzy Systems* 31, 11 (2023), 3995–4009. https://doi.org/10.1109/TFUZZ.2023.3273308